crystals

MDPI

Article

Transient Thermophysical Response of Al_2O_3 Nanoparticle-Loaded Fluids in Thick-Walled Microtubes: Conjugate Heat Transfer and System-Level Thermal Filtering

Muhammed Said Ates

Department of Electricity and Energy, Vocational School of Technical Sciences, Bingol University, 12000 Bingöl, Türkiye; msates@bingol.edu.tr or msates@gmail.com

Abstract

Al_2O_3 nanoparticles are widely dispersed in heat-transfer fluids to form nanofluids with a tailored thermophysical response, because their addition modifies thermal conductivity, viscosity, heat capacity, and consequently the transient thermal behaviour of the fluid–solid system. In this study, the coupled effects of Al_2O_3 nanoparticle loading and solid-wall thickness on the transient response of a thick-walled microtube heated over a finite length at low flow rate, as in heated microfluidic devices, are investigated by numerical simulation. A finite-volume conjugate model with Navier slip is solved directly in the time and frequency domains, with quantified grid and time-step uncertainty. For a wall with ten times the volumetric heat capacity of water, raising the wall-to-radius ratio from 0.2 to 1.0 lengthens the 99% response time 17-fold, lowers the cut-off frequency 14-fold and conducts 28% of the heat upstream of the heater; for glass and PDMS walls the response time grows only 2–3-fold. This attenuation is capacitive and system-level; up to $\omega = 0.1$ the trans-wall transfer function stays above 0.99. Loading up to 10 vol% shortens the response time by 5–17% at fixed Peclet number; at constant flow rate it raises the heat transfer coefficient by 32% but, under the Maiga correlations, nearly triples the pumping power.

Keywords: transient conjugate heat transfer; nanofluids; Al_2O_3-water nanofluid; nanoparticles; thermophysical properties; wall thickness ratio; thermal response time; frequency response

1. Introduction

Microfluidic devices increasingly carry their own thermal functions: lab-on-chip systems with integrated heaters, micro-reactors and sensor packages control the temperature of small liquid volumes, and microfluidic channels are now also used for the thermal regulation of compact and flexible electronics [1]. In such devices, a resistive heater or a heat-dissipating component is often bonded to a short length of a channel or tube wall, for temperature control or for thermal flow sensing [2], and the liquid passes at flow rates of the order of microlitres per minute. Since the heater does not touch the liquid, the heat reaches the liquid through the wall, which stores part of the heat, conducts part of it along the tube and delays the rest. Microchannel cooling goes back to the heat sinks of

Academic Editor: George D. Verros

Received: 24 September 2026
Revised: 1 November 2026
Accepted: 2 November 2026
Published: 6 November 2026

Copyright: © 2026 by the author. Licensee MDPI, Basel, Switzerland. This article is an open access article distributed under the terms and conditions of the Creative Commons Attribution (CC BY) license.

Tuckerman and Pease [3]; the present study concerns the low-flow end of this range, where conduction in the wall is as important as convection to the liquid.

Nanofluids, colloids of a base liquid and metal-oxide nanoparticles such as Al_2O_3, CuO or TiO_2, are a common means of raising the thermal conductivity of the liquid; alumina-water nanofluids in particular have been widely studied for their chemical stability, ease of dispersion and cost [4–9]. The enhancement is set by the dispersed particles themselves: their size [10,11] and shape [12], together with temperature [7], change the effective conductivity and viscosity of the suspension. Continuum models see these particle characteristics only through effective-property correlations, so the choice of correlation, and the concentration range over which it was fitted to experiment, directly shapes the predicted thermal performance [13,14]. The addition of nanoparticles also raises the viscosity, more steeply than the conductivity at moderate concentrations, so that the pumping power and the viscous heating grow with loading [15]; in Al_2O_3-water microchannel flow, viscous dissipation has been found to reduce the heat-transfer gain of the nanofluid more strongly as the Reynolds number rises [16].

At the microscale, the heat generated by viscous shear, characterised by the Brinkman number (Br), can act as a volumetric heat source that alters the temperature field and the Nusselt number [17–20], and it remains part of current analyses of fully developed microchannel flow [21]; with nanofluids, the viscosity increase amplifies it [13]. Its importance, however, depends on the dimensional operating point, which is therefore established before Br is chosen (Section 2.4). Liquid flow in microtubes may in addition exhibit apparent wall slip [22,23].

A further feature of microscale heat transfer is conjugation with the wall. In microtubes, the wall thickness is often comparable to or larger than the fluid radius ($d^* = d_w/R_i \sim 1$), so heat conducts within the wall in both radial and axial directions. The extended Graetz problem with wall conduction, and axial wall conduction more generally, has been studied for both channels and tubes [24–27]. When axial conduction dominates, the interfacial heat flux becomes skewed and the local Nusselt number non-uniform, which can also bias the reduction of experimental data [28]. At low Reynolds numbers, axial conduction carries heat upstream of the heated section; this back axial conduction has been investigated experimentally in nanofluid-cooled microchannel heat sinks [29]. The resulting upstream preheating warms the entering fluid before it reaches the heated section and modifies both the interface heat flux and the thermal development length. The role of wall thickness and wall material in conjugate microchannel heat transfer has also been examined for flow boiling [30].

Real devices frequently operate under transient conditions: heater start-up, pulsed loads, and periodic duty cycles. The transient conjugate problem has been treated for fully developed and developing pipe flows [31–33], including thick-walled pipes with two-dimensional wall conduction [34–37] and straight microchannels [38]. Under time-varying loads, the thermal capacity of the wall becomes part of the dynamics; its influence on the coupling between wall temperature and flow oscillations has been analysed for microchannel flow boiling [39]. Time-periodic forcing of nanofluid flows has mostly been studied through oscillatory flow conditions [40], and transient conjugation under a time-periodic wall temperature has been analysed for thick-walled pipes and minipipes by Altun et al. [41]. The response of a thick wall to a modulated heat input is also what an outer-surface sensor sees: estimating the inner state from outer measurements is the classical inverse heat-conduction problem [42], increasingly addressed with machine-learning surrogates [43].

Despite this literature, the combined transient behaviour of a thick conjugate wall, nanofluid properties, and wall slip under both step and harmonic heating has received little attention, and three specific questions motivate this work. First, how strongly does

the wall thickness, compared with the nanoparticle loading, control the transient lag, and how does this depend on the wall material and the Peclet number? Second, parametric studies commonly vary Pe, Br and ϕ independently, whereas in a loop operated at a fixed flow rate these groups are coupled through the nanofluid properties; what are the transient, heat-transfer and pumping consequences at such coupled operating points? Third, how much of the attenuation of a modulated heater signal is due to the wall itself (trans-wall filtering) and how much to the assembly as a whole (system-level filtering)?

To address these questions, this work presents a numerical investigation of transient conjugate heat transfer of an Al_2O_3-water nanofluid in a thick-walled microtube heated over a finite length. The specific objectives are:

1. To quantify how the wall thickness ratio (d^*) and the Al_2O_3 volume fraction (ϕ), acting through the thermophysical properties of the mixture, affect the transient temperature field and a solver-independent thermal response time (τ_p^*), and how these effects depend on the wall material and Pe.
2. To analyse the upstream preheating by axial wall conduction and its consequences for the interface heat flux and the Nusselt number.
3. To separate system-level and trans-wall thermal filtering by driving the outer surface with a sinusoidal heat flux and computing the transfer functions directly in the frequency domain.
4. To simulate the coupled operating points of a constant-flow-rate loop and to quantify the pumping-power penalty.

Section 2 describes the configuration, the assumptions, the governing equations, and the verified numerical method. Section 3 presents the results, and Section 4 summarises the conclusions.

2. Mathematical Formulation

2.1. Physical Configuration, Target Application, Modelling Assumptions and Scope

We consider transient conjugate heat transfer in an infinitely long microtube in axisymmetric cylindrical coordinates (x^*, r^*) (Figure 1; the symbols are listed in Appendix A):

- The fluid domain occupies $0 \le r^* \le 1.0$.
- The solid wall occupies $1.0 < r^* \le 1.0 + d^*$, where $d^* = d_w/R_i$ is the wall thickness ratio (d_w the dimensional wall thickness, R_i the inner radius; d_w is used to avoid confusion with the diameter D_i).
- The outer wall ($r^* = 1.0 + d^*$) is heated over a localised section of dimensionless length $L^* = 7.68$ ($x^* \in [0, L^*]$) by a uniform heat flux q''; the rest of the outer wall is insulated.
- Flow enters from upstream infinity ($x^* \to -\infty$) and exits to downstream infinity ($x^* \to +\infty$).

The configuration represents a heated section of a liquid-cooled microtube operating at low flow rates, as encountered in microfluidic thermal management: lab-on-chip devices with integrated heaters, micro-reactors and sensor packages, in which a resistive heater or a heat-dissipating component is bonded to a short length of the tube wall. The low Peclet number of the baseline ($Pe = 5$, i.e., $Re_D = Pe/Pr_{nf} \approx 0.7$ for the baseline nanofluid) makes axial conduction in both the fluid and the wall significant, which is the regime in which wall conjugation and its transient lag are most pronounced. Representative dimensional scales are given in Section 2.4 and Appendix B.

The model rests on the following assumptions:

1. **Laminar, incompressible, Newtonian flow.** At the baseline, the Reynolds number based on the inner diameter is $Re_D = Pe/Pr_{nf} \approx 0.7$ ($Pr_{nf} = 7.5$ at $\phi = 0.02$), far below the laminar limit.
2. **Hydrodynamically fully developed, steady flow.** The velocity field is established before the heating is switched on and is independent of x and t; only the temperature field is developing (thermal-entry, or extended Graetz, problem [26,35,36]).
3. **Constant (temperature-independent) properties** of the fluid and the wall, evaluated at a single reference temperature. The momentum and energy equations are therefore decoupled, and the energy equations are linear in temperature (used in Section 3.3).
4. **Homogeneous single-phase nanofluid.** The particles and the base fluid are in local thermal and mechanical equilibrium, and the mixture is described by effective properties (Section 2.4), as in [13,15]; particle migration and two-component effects [5] are outside the present scope.
5. **Axisymmetry.** The heating is uniform around the circumference, and there is no swirl.
6. **Negligible body forces.** Gravity (buoyancy) and electromagnetic forces are neglected (Section 2.2.1).
7. **Viscous dissipation retained** (Section 2.2.1).
8. **Radiation neglected.** With a linearised radiation coefficient of about 6 W/(m² K) at 300 K [44], a black outer surface 33 K above its surroundings, the warmest case of Table A4, would lose about 0.02 W/cm², i.e., 2% of the heater flux $q'' = 1$ W/cm².
9. **No internal heat generation in the wall.**
10. **Liquid wall slip** of the Navier type (Section 2.2.1); no temperature jump at the wall, and perfect thermal contact between the fluid and the wall (no interfacial thermal resistance). The Kapitza length of water–solid interfaces, 3–12 nm [45], is at least three orders of magnitude below the tube radii considered (25–100 µm).
11. **Axial conduction retained in both the fluid and the wall**, as required at low Pe [25,26,36].

The infinite domain is truncated to $[x^*_{in} = -23.04,\ x^*_{out} = 23.10]$, with unheated inlet and outlet lengths large enough that the inlet and developed-outlet conditions at infinity are asymptotically satisfied (Sections 2.3 and 2.6.1).

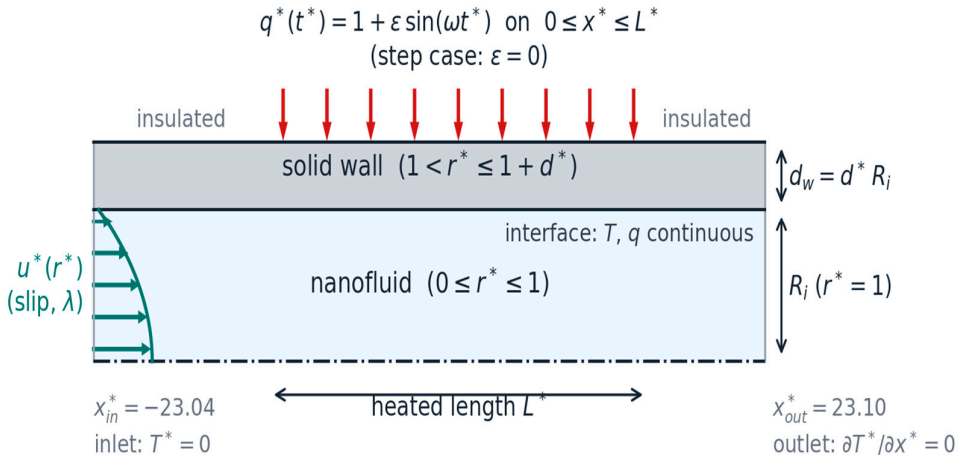


Figure 1. Schematic of the axisymmetric computational domain (not to scale): nanofluid core ($0 \le r^* \le 1$), solid wall ($1 < r^* \le 1 + d^*$), outer surface heated over $0 \le x^* \le L^*$ with $q^*(t^*) = 1 + \varepsilon\sin(\omega t^*)$ ($\varepsilon = 0$ for step cases) and insulated elsewhere; slip (Navier) velocity profile at the inlet.

2.2. Governing Equations

2.2.1. Fluid Domain ($0 \le r^* \le 1.0$)

Vector form. For an incompressible Newtonian fluid with constant properties, mass, momentum, and energy conservation, see [5,13,46]

$$\nabla \cdot \boldsymbol{u} = 0, \tag{1}$$

$$\rho_{nf}\left(\frac{\partial \boldsymbol{u}}{\partial t} + \boldsymbol{u} \cdot \nabla \boldsymbol{u}\right) = -\nabla P + \mu_{nf}\nabla^2 \boldsymbol{u} + \boldsymbol{f}_b, \tag{2}$$

$$(\rho C_p)_{nf}\left(\frac{\partial T}{\partial t} + \boldsymbol{u} \cdot \nabla T\right) = \nabla \cdot \left(k_{nf}\nabla T\right) + \mu_{nf}\,\Phi_v, \tag{3}$$

where P is the pressure, $\boldsymbol{f}_b$ collects the body forces per unit volume and $\mu_{nf}\Phi_v$ is the rate of viscous dissipation, with $\Phi_v = 2\,\boldsymbol{D}\!:\!\boldsymbol{D}$ and the rate-of-strain tensor $\boldsymbol{D} = 1/2\,(\nabla \boldsymbol{u} + \nabla \boldsymbol{u}^{\mathrm{T}})$.

Body forces. The only body force that could act is gravity, $\boldsymbol{f}_b = \rho_{nf}\boldsymbol{g}$. Its hydrostatic part is absorbed into the pressure; its thermal part (buoyancy, $-\rho_{nf}\beta(T - T_{in})\boldsymbol{g}$ in the Boussinesq form) drives mixed convection only when the Richardson number $Ri_D = Gr_D/Re_D^2$ is not small, with $Gr_D = |\boldsymbol{g}|\,\beta\,(T_{iw} - T_b)\,D_i^3/\nu_{nf}^2$ based on the wall-to-bulk temperature difference. For the representative scales of Section 2.4 ($D_i = 100$ µm, $q'' = 1$ W/cm², $T_{iw} - T_b \approx 0.4$ K) and the expansion coefficient of water at the reference temperature of Section 2.4 ($\beta = 2.07 \times 10^{-4}$ K⁻¹ at 20 °C [47]), $Gr_D \approx 7 \times 10^{-4}$ and $Ri_D \approx 1.5 \times 10^{-3}$. Because Re_D is fixed by Pe while $T_{iw} - T_b$ scales with $q''D_i$, Ri_D grows as $q''D_i^4$; buoyancy therefore remains negligible ($Ri_D \le 0.024$) for $D_i \lesssim 200$ µm at $q'' \le 1$ W/cm², which bounds the applicability of the present forced-convection model. No electric or magnetic fields are applied, so electromagnetic forces are absent. Hence $\boldsymbol{f}_b$ does not enter the reduced equations.

Reduction. Under assumptions 1–5 of Section 2.1, the velocity is purely axial and depends on r only, $\boldsymbol{u} = u(r)\,\boldsymbol{e}_x$. Continuity is then satisfied identically, $\boldsymbol{u} \cdot \nabla \boldsymbol{u} = 0$, and the axial momentum equation reduces to

$$\frac{\mu_{nf}}{r}\frac{\mathrm{d}}{\mathrm{d}r}\left(r\frac{\mathrm{d}u}{\mathrm{d}r}\right) = \frac{\mathrm{d}P}{\mathrm{d}x} = \text{const}, \tag{4}$$

subject to symmetry, $\mathrm{d}u/\mathrm{d}r = 0$ at $r = 0$, and the Navier slip condition at the wall [19,22–24],

$$u_{slip} = u(R_i) = -b\left.\frac{\mathrm{d}u}{\mathrm{d}r}\right|_{r=R_i}, \qquad b = \lambda R_i. \tag{5}$$

Integrating twice and normalising with the mean velocity u_m gives the slip-corrected Hagen–Poiseuille profile

$$u^*(r^*) = \frac{u}{u_m} = \frac{2\,(1 - r^{*2} + 2\lambda)}{1 + 4\lambda}, \tag{6}$$

which recovers the no-slip profile $2(1 - r^{*2})$ as $\lambda \to 0$; the normalisation $(1 + 4\lambda)$ yields a non-negative wall velocity $u^*(1) = 4\lambda/(1 + 4\lambda)$ for $\lambda > 0$.

Slip model. Wall slip is included because liquid flow in microtubes can exhibit apparent wall slip arising from surface effects rather than gas-like rarefaction [22,23], so a Knudsen-number criterion does not apply here. With the slip length $b = \lambda R_i$, $\lambda = 0.01$ corresponds to a slip length of one per cent of the tube radius, and the classical no-slip profile is recovered continuously as $\lambda \to 0$. The effect of slip on heat transfer is small: at $\lambda = 0.01$ the fully developed Nusselt number is only 2.1% above its no-slip value (4.4565 against $48/11 = 4.3636$). Because the dependence of the slip length on particle loading remains an open question for nanoparticle-loaded liquids, the slip coefficient is

held at $\lambda = \lambda_0 = 0.01$ for all concentrations, which attributes no change in slip to the particles. Two concentration-dependent alternatives were tested as a sensitivity ($Br = 0$, $\phi = 0.001$–0.10, $d^* = 0.2$ and 1.0). The first, $\lambda = \lambda_0\, \mu_{nf}/\mu_{bf}$, follows from Navier's condition, in which the wall shear stress is balanced by an interfacial friction $\kappa\, u_{slip}$, so that $b = \mu/\kappa$, if the friction coefficient κ does not change with loading. The second, $\lambda = \lambda_0\, (\mu_{nf}/\mu_{bf})/(\rho_{nf}/\rho_{bf})$, scales the slip length with the kinematic viscosity; it is the slip condition of two-phase nanofluid models [48,49], also used in [43], in which the slip length is the kinematic viscosity multiplied by a slip velocity factor that is taken to be independent of the loading. At $\phi = 0.10$, they raise λ to 0.030 and 0.023 and the fully developed Nusselt number by 3.8% and 2.5%, but change the concentration effect on the steady inner-wall temperature and on the response time τ^*_{99} (Section 3.1.3) by at most 0.3 percentage points.

For this unidirectional flow, the dissipation function contains a single term, $\Phi_v = (\mathrm{d}u/\mathrm{d}r)^2$, and the energy equation becomes

$$(\rho C_p)_{nf}\left(\frac{\partial T}{\partial t} + u\frac{\partial T}{\partial x}\right) = k_{nf}\left[\frac{\partial^2 T}{\partial x^2} + \frac{1}{r}\frac{\partial}{\partial r}\left(r\frac{\partial T}{\partial r}\right)\right] + \mu_{nf}\left(\frac{\mathrm{d}u}{\mathrm{d}r}\right)^2. \tag{7}$$

The axial conduction term is retained because it is of order Pe^{-2} relative to radial conduction and is not negligible at low Pe [25,26].

Non-dimensionalisation. Following the reference conjugate formulation [36], we introduce

$$r^* = \frac{r}{R_i}, \quad x^* = \frac{x}{R_i\, Pe}, \quad t^* = \frac{\alpha_{nf}\, t}{R_i^2}, \quad T^* = \frac{T - T_{in}}{\Delta T_{ref}}, \quad \Delta T_{ref} = \frac{q'' R_i}{k_{nf}}, \tag{8}$$

$$Pe = \frac{2\, u_m R_i}{\alpha_{nf}}, \quad Br = \frac{\mu_{nf}\, u_m^2}{k_{nf}\, \Delta T_{ref}} = \frac{\mu_{nf}\, u_m^2}{q'' R_i}. \tag{9}$$

Throughout the paper, a superscript asterisk (*) denotes a dimensionless quantity. The Peclet number is diameter-based, written with the inner radius for consistency with the remaining scales, and the Brinkman number is defined with the constant-flux temperature scale ΔT_{ref} of the present non-dimensionalisation, consistent with the definition used in the companion formulation [43]. Dividing the energy equation by $k_{nf}\Delta T_{ref}/R_i^2$, the transient term becomes $\partial T^*/\partial t^*$; the convective term becomes $(R_i u_m/\alpha_{nf})\,(u^*/Pe)\,\partial T^*/\partial x^* = (u^*/2)\,\partial T^*/\partial x^*$, because the diameter-based Pe carries the factor 2; the axial conduction term acquires the factor Pe^{-2} from the Graetz scaling of x; and the dissipation term becomes $Br\,\Phi^*$ with $\Phi^* = (\mathrm{d}u^*/\mathrm{d}r^*)^2$. The result is the dimensionless energy equation of the fluid,

$$\frac{\partial T^*}{\partial t^*} + \frac{u^*(r^*)}{2}\frac{\partial T^*}{\partial x^*} = \frac{1}{Pe^2}\frac{\partial^2 T^*}{\partial x^{*2}} + \frac{1}{r^*}\frac{\partial}{\partial r^*}\left(r^*\frac{\partial T^*}{\partial r^*}\right) + Br\cdot\Phi^*, \qquad \Phi^* = \frac{16\, r^{*2}}{(1+4\lambda)^2}, \tag{10}$$

which is the formulation of [36] extended by the slip profile and the dissipation term of [19,24]. The conjugate-solver lineage follows the thick-walled-pipe formulation of Bilir and Ateş [50] and the conjugate-microtube treatment of [24].

2.2.2. Solid Domain ($1.0 < r^* \le 1.0 + d^*$)

In vector form, the wall obeys transient conduction without internal heat generation,

$$(\rho C_p)_s\,\frac{\partial T}{\partial t} = \nabla\cdot(k_s \nabla T), \tag{11}$$

which, with the same scales as the fluid (so that both domains share T^*, x^*, r^* and t^*), becomes

$$\frac{\partial T^*}{\partial t^*} = \alpha_{wnf}\left[\frac{1}{Pe^2}\frac{\partial^2 T^*}{\partial x^{*2}} + \frac{1}{r^*}\frac{\partial}{\partial r^*}\left(r^*\frac{\partial T^*}{\partial r^*}\right)\right], \qquad \alpha_{wnf} = \frac{\alpha_s}{\alpha_{nf}}$$
$$= \alpha_{sf}\cdot\frac{(\rho C_p)_{nf}}{(\rho C_p)_{bf}}\cdot\frac{k_{bf}}{k_{nf}}, \qquad \alpha_{sf} = \frac{\alpha_s}{\alpha_{bf}}. \tag{12}$$

Here α_{wnf} appears because time is scaled with the fluid diffusivity [36].

2.3. Initial, Boundary and Interface Conditions

1. **Initial condition ($t^* = 0$):** Before the heating starts, the nanofluid already flows with its fully developed velocity profile, and the fluid and the wall are at the uniform inlet temperature, $T^* = 0$ in both domains. At $t^* = 0$ the uniform heat flux is suddenly applied over the heated section of the outer wall and is held constant thereafter. Physically, this is the start-up of a heater on a tube that is in thermal equilibrium with the coolant; it is the sudden-heating input of the reference conjugate study [36] and defines the response times of Section 3.1.3.
2. **Numerical inlet ($x^*_{in} = -23.04$; Figure 1):** $T^* = 0$ in the fluid and the wall. The coolant arrives from an upstream reservoir at T_{in}. The inlet is placed 23.04 axial units upstream of the heated section so that the upstream preheating region created by axial conduction in the wall (Section 3.1.2) decays before reaching it; Section 2.6.1 shows that moving it further upstream does not change the results.
3. **Numerical outlet ($x^*_{out} = 23.10$; Figure 1):** $\partial T^*/\partial x^* = 0$ in the fluid and the wall. The outlet is 15.4 axial units downstream of the heated section, where the wall is adiabatic, and the axial conductive flux is negligible compared with the convective outflow; the condition only states that no heat is conducted across the outlet plane [36].
4. **Centreline ($r^* = 0$):** $\partial T^*/\partial r^* = 0$. With axisymmetric heating, no heat crosses the axis.
5. **Fluid–solid interface ($r^* = 1.0$):** $T^*_f = T^*_s$ and $\partial T^*_f/\partial r^* = k_{wnf}\,\partial T^*_s/\partial r^*$, with $k_{wnf} = k_s/k_{nf}$. The first condition expresses perfect thermal contact; the second is energy conservation across the interface: the heat conducted out of the wall equals the heat conducted into the fluid. Because both domains share the temperature scale, the physical continuity $k_{nf}\,\partial T_f/\partial r = k_s\,\partial T_s/\partial r$ reduces directly to this form [26,35,36]. In the present model, wall slip affects only the velocity and is not accompanied by a temperature jump (assumption 10).
6. **Outer wall ($r^* = 1.0 + d^*$):** $\partial T^*/\partial r^* = 1/k_{wnf}$ over the heated region $0 \le x^* \le L^*$, and $\partial T^*/\partial r^* = 0$ elsewhere. The first condition is Fourier's law for the prescribed flux q'' written in the fluid temperature scale; it models a heater or heat-dissipating component of uniform output. The adiabatic remainder isolates the redistribution of heat by wall conduction from external losses, so that the upstream and downstream leakage fractions of Section 3.1.4 are entirely due to axial conduction in the wall.

For the frequency-response study of Section 3.3, the heated-region flux condition is modulated in time as $q^*(t^*) = 1 + \varepsilon\sin(\omega t^*)$, i.e., condition 6 becomes $\partial T^*/\partial r^* = q^*(t^*)/k_{wnf}$ over the heated region.

2.4. Nanofluid Thermophysical Properties

The properties of the Al_2O_3-water nanofluid are evaluated with the Maiga et al. [13] correlations:

$$\frac{k_{nf}}{k_{bf}} = 1 + 2.72\phi + 4.97\phi^2, \qquad \frac{\mu_{nf}}{\mu_{bf}} = 1 + 7.3\phi + 123\phi^2, \tag{13}$$

$$\frac{(\rho C_p)_{nf}}{(\rho C_p)_{bf}} = (1-\phi) + \phi\frac{(\rho C_p)_p}{(\rho C_p)_{bf}}, \qquad \frac{\rho_{nf}}{\rho_{bf}} = (1-\phi) + \phi\frac{\rho_p}{\rho_{bf}}. \tag{14}$$

The viscosity relation is a least-squares fit to measured Al_2O_3-water viscosities (see the synthesis of Khanafer and Vafai [51]); the conductivity relation is compared with effective-medium theory below. The base fluid is water at room temperature (about 20 °C) and the particles carry bulk alumina properties: $\rho_{bf} = 998$ kg/m^3, $(C_p)_{bf} = 4186$ J/(kg K), $k_{bf} = 0.595$ W/(m K), $\rho_p = 3975$ kg/m^3, $(C_p)_p = 765$ J/(kg K) and $k_p = 36$ W/(m K) [44]. Only the ratios $\rho_p/\rho_{bf} = 3.98$ and $(\rho C_p)_p/(\rho C_p)_{bf} = 0.728$ enter the dimensionless model; k_p does not, because the empirical conductivity correlation already contains the particle contribution. Since the volumetric heat capacity of alumina is 27% below that of water, loading lowers $(\rho C_p)_{nf}$ slightly (-2.7% at $\phi = 0.10$) while raising k_{nf} by 32%; both raise the nanofluid diffusivity ($\alpha_{nf}/\alpha_{bf} = 1.36$ at $\phi = 0.10$), which is the particle-level origin of the Peclet shift of Section 3.4.

The steep quadratic viscosity term ($123\phi^2$) is the physically essential feature that distinguishes these correlations from dilute-limit models. A common simpler alternative combines the linear conductivity fit $k_{nf}/k_{bf} = 1 + 7.47\phi$ with the Batchelor viscosity $1 + 2.5\phi + 6.2\phi^2$ [52], which extends the suspension-rheology results of Einstein [53] and Brinkman [54]. The linear fit is commonly attributed to Pak and Cho [6]; it is consistent with the γ-Al_2O_3-water conductivity data they tabulate for $\phi = 0.013$–0.043, and later measurements at $\phi = 0.002$–0.008 reproduced it within 1.8% [55]. It is, however, not supported by classical effective-medium theory: for alumina particles ($k_p/k_{bf} \approx 60$), the Maxwell estimate [56], which coincides with the Hamilton–Crosser model [57] for spheres, gives $k_{nf}/k_{bf} = 1.316$ at $\phi = 0.10$, within 0.5% of the Maiga value (1.322), whereas the linear fit gives 1.747. An international benchmark on colloidally stable nanofluids likewise found measured conductivities in good agreement with effective-medium theory, with no anomalous enhancement [58]. These dilute-limit models overstate the conductivity gain and understate the viscosity penalty [6], and are experimentally justified only to $\phi \lesssim 0.06$. The size-dependent empirical correlations of Corcione [59] were also considered; for a representative particle diameter of 45 nm, however, their viscosity ratio reaches 4.5 at $\phi = 0.10$ (Maiga: 2.96) and diverges at $\phi \approx 0.13$, just beyond the present range; temperature-dependent enhancement [7] is outside the present single-reference-temperature scope. The concentration sweep in this study is restricted to $\phi \in [0.001, 0.10]$.

Validity at the highest loadings. The property model is the main source of model uncertainty at the highest concentrations, and its parts enter the results differently. The conductivity relation lies within 0.5% of the Maxwell estimate at $\phi = 0.10$ (above), so it is not sensitive to extrapolation. The viscosity relation, whose quadratic term dominates at $\phi = 0.10$, is the most uncertain input; comparisons of existing Al_2O_3-water property models with experiments show that the best-performing pair of viscosity and conductivity models changes with concentration even for $\phi \leq 0.04$ [14]. With the concentration-independent slip coefficient of Section 2.2.1, however, the viscosity does not enter the thermal results at $Br = 0$; it affects only the pumping power (Section 3.4) and, because $Br \propto \mu_{nf}$, the dissipation term, which matters only in the high-dissipation limit (Section 3.6). The temperature dependence of the properties is excluded by the moderate-heating window discussed below. The viscosity correlation and the pumping power of Section 3.4 also presume Newtonian behaviour: well-dispersed Al_2O_3-water suspensions have been measured to be Newtonian up to 5 vol%, whereas aggregated ones become shear-thinning [60]. Finally, the stability of the dispersion, which decides whether the particles remain suspended in a real device [61], is not modelled; the results at the highest concentrations are therefore model predictions for a stable, well-dispersed suspension.

Representative dimensional scales. The baseline groups are related to physical conditions through $u_m = Pe\,\alpha_{nf}/D_i$, $\Delta T_{ref} = q''R_i/k_{nf}$ and $Br = \mu_{nf}u_m^2/(q''R_i)$ (Table A4, Appendix B). For the baseline nanofluid ($\phi = 0.02$, $Pr_{nf} = 7.5$), $Pe = 5$ corresponds to $Re_D = 0.67$ and to mean velocities of 3.8–15 mm/s in tubes of $D_i = 200$–50 µm, i.e., volumetric flow rates of 1.8–7.1 µL/min; these channel radii and this Reynolds number lie within the ranges typical of microfluidic devices [62]. With a heater flux of $q'' = 1$ W/cm², the reference temperature scale is 0.4–1.6 K and the Brinkman number is 10^{-8}–10^{-6}, so viscous dissipation is negligible in this window; the main results are therefore computed with $Br = 0$, and $Br = 0.01$ is treated separately as a high-dissipation limit (Section 3.6). Because the model is linear, dimensional temperatures scale with q''. The steady mean inner-wall temperature rise over the heated section is $\Delta T_{iw} \approx 21\,q''R_i/k_{nf}$ ($d^* = 0.2$), about 17 K for $D_i = 100\,\mu$m and $q'' = 1$ W/cm². Since the viscosity of water falls by about 2% per kelvin near room temperature [63], the constant-property assumption restricts the model to moderate heating, e.g., $q'' \lesssim 0.3$ W/cm² at $D_i = 100\,\mu$m for $\Delta T_{iw} \approx 5$ K; within this window the dimensionless results hold for any q''.

2.5. Analytical Operational Coupling

To bridge independent numerical sweeps and physical experiments, we note that in a real loop the pump fixes the inlet velocity u, so varying ϕ shifts the active Pe and Br through the fluid properties:

$$Pe(\phi) = Pe_0 \cdot \frac{(\rho C_p)_{nf}(\phi)}{(\rho C_p)_{bf}} \cdot \frac{k_{bf}}{k_{nf}(\phi)}, \qquad Br(\phi) = Br_0 \cdot \frac{\mu_{nf}(\phi)}{\mu_{bf}}. \tag{15}$$

The Brinkman shift is purely viscous: at fixed u and q'' the k_{nf} of the Brinkman definition cancels against the k_{nf} of the temperature scale ΔT_{ref}, leaving $Br = \mu_{nf}\,u_m^2/(q''R_i)$ (Section 2.2.1), so the conductivity gain enters the operating point only through Pe. Here Pe_0 and Br_0 are the values for the pure base fluid ($\phi = 0$); with $Pe_0 = 5$, the constant-velocity trajectory passes $Pe = 4.71$ at the baseline loading $\phi = 0.02$. Section 3.4 reports simulations along these constant-velocity trajectories.

2.6. Numerical Method and Verification

Three complementary safeguards separate the physical conclusions of Section 3 from numerical artefacts. First, all transient results are reported through threshold-based response times τ_p^* (Section 3.1.3) rather than the solver's steady-state termination time: the termination time is a by-product of the convergence tolerance and the adaptive time-step policy, and is therefore neither physical nor reproducible across codes, whereas τ_p^* depends only on the computed temperature history. Second, the error of the iterative inner solver is quantified by a tolerance study and removed altogether by solving the identical discrete equations directly (Section 2.6.2). Third, the discretisation error remaining in the computed histories is quantified with grid-convergence-index (GCI) studies in time and space (Section 2.6.3), so reported quantities carry a stated numerical uncertainty. Iterative, temporal and spatial errors are thus assessed separately, as recommended for code and solution verification [64,65].

2.6.1. Mesh and Discretisation

The domain is discretised on a uniform axisymmetric grid. Axially, $\Delta x^* = 0.06$ over $[-23.04, 23.10]$ ($N_x = 770$ axial nodes in total; $N_{x,in} = 384$ inlet, $N_{x,h} = 128$ heated and $N_{x,out} = 256$ outlet control volumes, plus the inlet node and one outflow boundary cell). Radially, the fluid domain is divided into $N_{r,f} = 16$ uniform cells ($\Delta r_f^* = 0.0625$). For the solid wall, the number of radial cells $N_{r,s}$ is scaled with the wall thickness, $N_{r,s} = \mathrm{round}(8\,d^*/0.2)$ (i.e., $N_{r,s} = 8, 16, 32, 40$ for $d^* = 0.2, 0.4, 0.8, 1.0$), which keeps the solid

radial cell size $\Delta r_s^* = d^*/N_{r,s} \approx 0.025$ approximately constant across the sweep, so that the radial resolution of the wall does not degrade with its thickness.

The equations are discretised with a vertex-centred finite-volume method on these grids: every node carries a control volume bounded by the mid-planes to its neighbours, and the interface nodes lie on the fluid–solid boundary $r^* = 1$. Diffusive fluxes in both directions use second-order central differences. The axial convection term is also discretised with central differences (linear interpolation of the face temperatures, second order on the uniform grid); the face mass flux of each control volume is the exact integral of the slip velocity profile over its radial extent, $\int (u^*/2)\, r^*\, \mathrm{d}r^*$, so that the discrete flow rate equals the analytical one. With $\Delta x^* = 0.06$ the largest cell Peclet number is $Pe^2\, \Delta x^*\, u_{max}^*/2 = 1.47$ at $Pe = 5$, below the bound of 2, so all neighbour coefficients are positive and the central scheme is bounded without upwinding; for the sensitivity runs at $Pe = 10$ the axial step is reduced to $\Delta x^* = 0.015$, which keeps the same value. The control volume of an interface node straddles the boundary: its fluid half $[1 - \Delta r_f^*/2,\ 1]$ carries the fluid capacity, the convective flux of the slip profile and the viscous dissipation, and its solid half $[1,\ 1 + \Delta r_s^*/2]$ the wall capacity, each with its own conductivity; the radial fluxes on either side use the conductivity of their own material, so the continuity conditions of Section 2.3 are satisfied by the control-volume balance itself, without an interfacial conductivity average. The nodes on the outer wall carry half control volumes, $[1 + d^* - \Delta r_s^*/2,\ 1 + d^*]$; their heat capacity, the conduction through their inner face and the applied flux are all balanced over this half volume. The heater ends $x^* = 0$ and $x^* = L^*$ lie on nodes whose control volumes are only half heated; these nodes receive half the flux, so that the heat input equals the nominal value $(1 + d^*)L^*$ on every grid. These interface, outer-wall, and heater-end control volumes are sketched in Figure A1 (Appendix C). Temporal integration is fully implicit (backward Euler, first order).

The discretised system is marched in time with a GPU-accelerated CUDA Jacobi relaxation solver (relaxation factor 1.0, i.e., unaccelerated Jacobi). Because the axisymmetric problem is small ($1.9–4.4 \times 10^4$ unknowns on the production grid, 3.0×10^5 on the finest), the same discrete equations are also assembled into a sparse matrix and solved directly by sparse LU factorisation (SciPy/SuperLU [66,67]); the coefficient arrays, boundary treatment and interface closure are identical in both routes. The direct solution differs from the Jacobi solution only in the absence of inner-iteration error; it serves as the converged reference of Section 2.6.2 and as the source of the results reported in Section 3. The code and the data underlying all figures and tables are openly available [68].

Domain length. At the baseline, doubling the outlet length or moving the inlet from $x_{in}^* = -23.04$ to -46.08 leaves the heated-section quantities of the thin wall ($d^* = 0.2$) unchanged to all reported digits; for the thick wall ($d^* = 1.0$), which has the longest upstream preheating region, the inlet shift changes τ_{99}^* by 0.04% and the steady inner-wall temperature by 0.004%, and the outlet extension changes τ_{99}^* by 0.13%. Cases with longer preheating regions were run with a longer inlet section, chosen in the same way: $x_{in}^* = -46.08$ for the stainless-steel walls at $d^* \geq 0.4$ and for the coupled operating points at $d^* \geq 0.8$ (Section 3.4), and $x_{in}^* = -92.16$ for $Pe = 2.5$ at $d^* = 1.0$; a further doubling changes the steady inner-wall temperature by less than 0.03%. The high-dissipation limit is computed on the original domain, $x_{in}^* = -11.52$ (Section 3.6).

2.6.2. Time Stepping and Iterative Convergence

The initial time step is $\Delta t_0^* = 10^{-4}$; whenever a step requires more than one inner iteration, it is grown by the factor $g = 1.01$, so that $\Delta t^* \approx \Delta t_0^* + (g - 1)\, t^*$. At the times of interest, the step size is therefore set by the growth factor rather than by Δt_0^*, and $g - 1$ is the effective temporal-resolution parameter (Section 2.6.3). The transient is terminated when a step converges in a single inner iteration.

The Jacobi iteration stops when the maximum inter-iteration temperature change falls below an absolute tolerance δ_{it}. With large time steps, the iteration matrix has a spectral radius ρ_J close to unity, so the error left after stopping is of order $\delta_{\mathrm{it}}/(1-\rho_J)$ rather than δ_{it}; it accumulates in the slowest (axial, downstream) mode and lags the transient. A tolerance study at $d^* = 0.4$ ($\delta_{\mathrm{it}} = 10^{-6}, 10^{-7}, 10^{-8}$, compared with the direct solution of the identical discrete system; Table 1) shows this error decreasing linearly with δ_{it}. At $\delta_{\mathrm{it}} = 10^{-6}$, the heated-section steady temperatures are affected only at the 10^{-5} relative level, but the outlet temperature is 0.6% low, the step-response time τ^*_{99} is 1.5% too long, and in time-periodic runs the lag appears as a spurious component at the forcing frequency that does not scale with the forcing amplitude, reducing the inner-wall oscillation amplitude by 7.6%. At $\delta_{\mathrm{it}} = 10^{-8}$ the deviations fall to 0.01% (τ^*_{99}) and 0.05% (amplitude). All quantities reported in Section 3 are therefore evaluated from the direct solution of the discrete equations, that is, in the limit where the iteration error vanishes entirely, using the same time-step sequence for transients; the GPU solver at $\delta_{\mathrm{it}} = 10^{-8}$ reproduces them to within 0.05%.

Table 1. Verification summary. Columns L1–L4 give the four levels of each study; the production level is in bold. Iterative study: $\delta_{\mathrm{it}} = 10^{-6}/10^{-7}/10^{-8}$ and the direct solution ($d^* = 0.4$, $\omega = 0.02$; on the original domain $x^*_{in} = -11.52$ of the GPU runs, so that both solvers treat an identical discrete system). Temporal study: $g - 1 = 0.04/0.02/0.01/0.005$ ($d^* = 0.2$). Spatial study: coarse/medium/fine/x-fine grids ($d^* = 0.2$ unless stated; response times and ω_c on three grids). p and Limit: observed order and Richardson-extrapolated value from the three finest levels, or the exact or direct value; osc.: oscillatory convergence. U_{prod}: uncertainty of the production level, $F_s\,|L_{prod} - \mathrm{Limit}|/L_{prod}$ with $F_s = 1.25$ [64,65], or, for oscillatory convergence, the difference between the production and the finest level.

Study	Quantity	L1	L2	L3	L4	p	Limit	U_{prod}
Iterative	τ^*_{99}	371.74	366.89	366.43	**366.38**	—	366.38 (direct)	—
Iterative	$\lvert H_{\mathrm{sys}}\rvert$ ($\omega = 0.02$)	0.4399	0.4731	0.4758	**0.4760**	—	0.4760 (direct)	—
Temporal	τ^*_{99}	140.19	136.45	**134.59**	133.66	0.99	132.71	1.7%
Temporal	τ^*_{50}	29.15	29.07	**29.04**	29.02	1.00	29.00	0.2%
Spatial	T^*_{iw} (steady)	20.371	**20.748**	20.720	20.792	osc.	—	0.21%
Spatial	T^*_b (steady)	19.854	**20.239**	20.208	20.282	osc.	—	0.21%
Spatial	$Nu_{iw,fd}$ (solid side)	4.4145	**4.4460**	4.4539	4.4559	1.99	4.4566 (exact 4.4565)	0.30%
Spatial	$Nu_{iw,fd}$ (fluid side; comparison only)	4.771	**4.661**	4.572	4.517	0.72	4.434	6.1%
Spatial	C (solid side)	3.9742	**3.9916**	3.9963	3.9972	2.22	3.9975 (exact 4)	0.18%
Spatial	energy closure, % (solid side)	−0.170	**−0.045**	−0.011	−0.003	1.96	0 (exact)	—
Spatial	T^*_b @ $t^* = 1.4377$	0.5489	**0.5500**	0.5521	0.5521	osc.	—	0.37%
Spatial	τ^*_{99}, $d^* = 0.2$	132.94	**134.59**	134.33	—	osc.	—	0.19%
Spatial	τ^*_{99}, $d^* = 1.0$	2298.9	**2324.3**	2328.1	—	2.74	2328.8	0.24%
Spatial	$10^3\,\omega_c$, $d^* = 0.2$	30.28	**29.87**	29.96	—	osc.	—	0.29%
Spatial	$10^3\,\omega_c$, $d^* = 0.8$	3.569	**3.526**	3.525	—	5.13	3.525	0.05%

2.6.3. Temporal and Spatial Independence (GCI)

Time step. Because $\Delta t^* \approx \Delta t^*_0 + (g-1)\,t^*$, varying Δt^*_0 alone does not refine the step in the window of interest; the temporal study therefore varies the growth factor, $g - 1 = 0.04,0.02,0.01,0.005$ (refinement ratio $r = 2$), for $d^* = 0.2,0.4,0.8$ and 1.0 ($Pe = 5$, $Br = 0$, $\phi = 0.02$), using Roache's GCI [64] ($F_s = 1.25$; reporting per [65]). The observed order is $p = 0.97$–1.01, as expected for backward Euler. At the production setting $g = 1.01$ the uncertainty is 1.3–1.7% for τ^*_{99} and 0.2% for τ^*_{50}: absolute τ^*_{99} values are

biased high by the first-order scheme, whereas the ratio $\tau_{99}^*(d^*)/\tau_{99}^*(0.2)$ changes by less than 0.4% and the corresponding τ_{50}^* ratio by less than 0.1%. Steady-state quantities do not depend on the time-step policy.

Spatial mesh. A spatial refinement study was performed with four grids at ratio $r = 2$ (coarse/medium/fine/x-fine: $N_{r,f} = 8/16/32/64$ with matched axial and solid refinement; the medium grid is the production grid), holding the physical domain fixed ($d^* = 0.2$, $Br = 0$). Table 1 reports, for each quantity, the numerical uncertainty of the production grid, U_{prod}. Quantities derived from the interfacial flux converge at second order: the fully developed Nusselt number converges with $p = 1.99$ to 4.4566, within 0.01% of the analytic value 4.4565 obtained by quadrature of the fully developed energy equation for the implemented velocity profile (Section 2.2.1), and the energy-closure error, the deviation of $\int Q_{iw}^* \, \mathrm{d}x^*$ from the applied input $(1 + d^*)L^*$, converges to zero with $p = 1.96$. The steady heated-section temperatures converge in an oscillatory manner, the three finest grids lying within a 0.35% band and the production grid 0.21% below the finest grid. The response times and the cut-off frequency of Section 3.3 were evaluated on the coarse, medium and fine grids for a thin and a thick wall: τ_{99}^* converges with $p = 2.74$ at $d^* = 1.0$ ($U_{prod} = 0.24\%$) and differs by 0.19% between the production and the fine grid at $d^* = 0.2$, and ω_c is grid-independent to 0.05% at $d^* = 0.8$ and to 0.29% at $d^* = 0.2$. The production-grid uncertainty of every quantity reported in Section 3 is therefore at most 0.3%, well below the temporal uncertainty of τ_{99}^*.

The interfacial flux Q_{iw}^* is evaluated on the solid side of the interface, with a second-order one-sided difference in the purely conducting, finely resolved wall. A fluid-side backward difference over the nodes adjacent to the interface converges to the same limit, but only at first order and from above ($Nu_{iw,fd}$: 4.771/4.661/4.572/4.517, $p = 0.72$), placing the production-grid value 5% high; it is used only for the comparison with the reference solution in Section 2.6.4. The energy-consistency ratio $C = (\mathrm{d}T_b^*/\mathrm{d}x^*)/Q_{iw}^*$, whose theoretical value is 4 at $Br = 0$, converges to 3.9975 ($p = 2.22$). Table 1 summarises the verification.

Absolute quantities are reported with these uncertainties in mind; the paper's principal conclusions rest on ratios and trends that are robust to them.

2.6.4. Validation Against a Reference Conjugate Solution

The conjugate core of the solver, namely two-dimensional transient wall conduction, interface coupling, and axial conduction in both domains, is validated against the thick-walled pipe solution of Ateş, Darıcı, and Bilir [36], which solves the identical dimensionless problem in the classical (macro-scale) limit. Setting $\lambda = 0$, $Br = 0$ and $\phi = 0$ reduces the present formulation exactly to theirs (classical Poiseuille profile $u^* = 2(1 - r^{*2})$, no dissipation, base-fluid properties), and the two studies share the Graetz-scaled axial coordinate and the interface-to-outer-wall flux normalisation ($Q_{iw}^* = q_{iw}/q_{ow}$). For their reference case ($Pe = 5$, $d^* = 0.1$, $k_{sf} = 10$, $\alpha_{sf} = 1$), the transient axial distribution of the interfacial heat flux was compared at the six time levels of their Figure 2 ($t^* = 0.0719$–425.99). To avoid any circularity, the reference curves were digitised from the published figure independently of the present solution (connected-curve tracking, 78–103 points per curve). The present profiles were computed on four grids refined in all directions at ratio 2 ($N_{r,f} = 8/16/32/64$ with proportional wall and axial refinement) and are shown in Figure 2 both with the solid-side flux and with the fluid-side gradient of Section 2.6.3.

The comparison has three parts. (i) At the earliest time ($t^* = 0.0719$) and in the upstream preheating regions ($x^* < 0$), which are the signature of axial wall conduction, the profiles coincide with the reference (mean absolute deviation 0.0003 in Q_{iw}^* with the fluid-side gradient on the finest grid), confirming the axial and temporal scaling of the formulation. (ii) At steady state the solid-side flux equals the exact fully developed value

$1 + d^* = 1.10$ over the heated section, and the reference agrees with it to within 1% (mean deviation 0.010). (iii) At intermediate times the computed flux lies slightly above the reference curve. An exact result clarifies this difference: downstream of the heating onset the profile becomes axially uniform at intermediate times, so the applied heat is shared between the fluid and the wall in proportion to their heat capacities,

$$Q^*_{iw} = \frac{1 + d^*}{1 + (k_{sf}/\alpha_{sf})[(1 + d^*)^2 - 1]} = 0.3548, \quad (16)$$

independently of the discretisation and of the time scale. At $t^* = 5.31$ the solid-side flux reproduces this value on every grid (0.3608, 0.3565, 0.3554 and 0.3551), whereas the fluid-side gradient approaches it from below at first order (0.3114, 0.3330, 0.3440 and 0.3495). The digitised reference plateau (0.338) lies within the range of the fluid-side values on 16–32 radial fluid cells, so the remaining difference in Figure 2 is consistent with a fluid-side evaluation of the interface flux at moderate radial resolution. A pointwise comparison exactly at the heating onset ($x^* = 0$) is not meaningful, because the flux is singular there; the comparison is therefore made on full profiles.

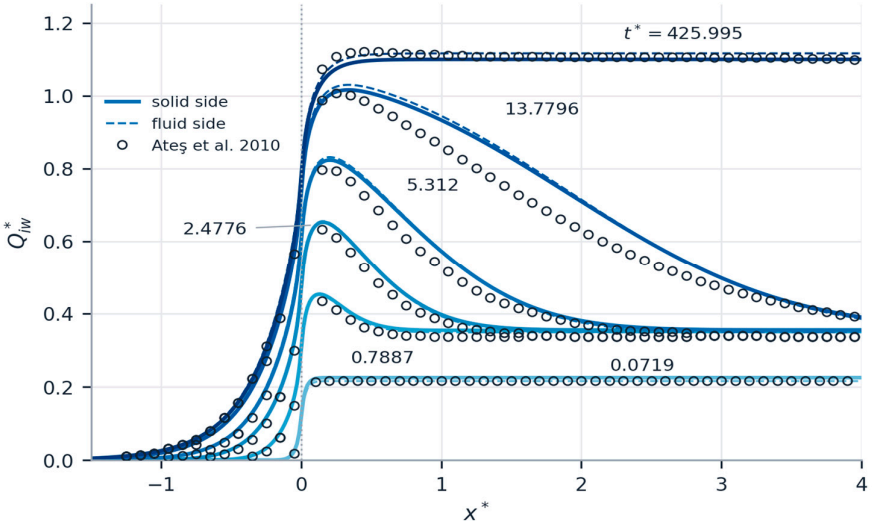


Figure 2. Validation against Ateş et al. [36]: transient axial interface heat-flux profiles at the six time levels of their Figure 2 ($Pe = 5$, $d^* = 0.1$, $k_{sf} = 10$, $\alpha_{sf} = 1$; $\lambda = Br = \phi = 0$ limit). Lines: present solution on the finest grid of the all-direction refinement ($N_{r,f} = 64$, $\Delta x^* = 0.015$); solid: solid-side interface flux; dashed: fluid-side gradient. Open symbols: reference curves digitised independently of the present solution.

The slip term of Section 2.2.1 vanishes identically in the $\lambda = 0$ limit used here, so this comparison isolates the conjugate core; the micro-scale extensions are verified separately: the fully developed Nusselt number converges to the analytic solution for the implemented slip profile (Section 2.6.3), the nanofluid property ratios are unit-tested against the Maiga correlations (Section 2.4), and the slip model is defined explicitly in Section 2.2.1.

2.7. Use of Generative Artificial Intelligence

Claude Code (Anthropic, version 2.1.207) and Google Antigravity IDE (Google, version 2.5.5) were used to assist with the development of the analysis, verification and visualisation scripts and with the writing and language editing of the manuscript. The numerical results were verified independently of these tools through the iterative, temporal and spatial error studies and the validation of Sections 2.6.2–2.6.4. The solver, the

verification and analysis scripts and the data underlying all figures and tables are openly available on Zenodo [68], so that the results can be checked independently of these tools. The author reviewed all code and text and takes full responsibility for the content.

3. Results and Discussion

The transient conjugate heat transfer of Al_2O_3-water nanofluid in the thick-walled microtube is analysed for the independent and coupled influences of the wall thickness ratio (d^*) and nanoparticle volume fraction (ϕ). Unless stated otherwise, the baseline is $Pe = 5,\ Br = 0,\ \phi = 0.02,\ d^* = 0.2$ (Section 2.4). Sections 3.1–3.4 use the generic solid–fluid pair of the reference conjugate study [36], $k_{sf} = 10$ and $\alpha_{sf} = 1$, whose volumetric heat capacity is ten times that of water; Section 3.5 repeats the main analyses for real wall materials and for $Pe = 2.5$ and 10, and Section 3.6 treats viscous dissipation as a high-dissipation limit ($Br = 0.01$).

3.1. Effect of Wall Thickness Ratio (d^*)

The wall thickness ratio $d^* = d_w/R_i$ sets both the radial thermal resistance and the heat capacity of the solid. Per unit length, the wall of the generic pair holds $(k_{wnf}/\alpha_{wnf})[(1 + d^*)^2 - 1] = 4.4$ times the heat capacity of the fluid core at $d^* = 0.2$ and 30 times at $d^* = 1.0$. The d^* sweep (0.2–1.0) shows how these two properties shape the transient.

3.1.1. Inner Interface vs. Outer Wall Temperature

Heat applied at the outer wall must cross the solid before reaching the interface, yet the heated-section-averaged outer-wall (T^*_{ow}) and interface (T^*_{iw}) temperatures rise almost together for every thickness (Figure 3a). Because the wall conducts much better than the nanofluid ($k_{wnf} \approx 9.5$), the radial drop across it is small: at steady state it is 0.022 ($d^* = 0.2$) to 0.120 ($d^* = 1.0$), that is, 0.11–0.27% of the inner-wall temperature, and it stays below the one-dimensional conduction estimate $(1 + d^*)\ln(1 + d^*)/k_{wnf}$ (0.023–0.146) because part of the heat is conducted axially. Figure 3b resolves the development of this drop on its own scale and shows two stages. In the first, the drop rises to a plateau at 49–58% of its steady value, reached at $t^* \approx 0.1$–0.35 and held until $t^* \approx 11$–56 (longer for thicker walls): the wall has reached its own radial conduction balance. In the second, the drop rises with the slow heating of the whole assembly and reaches 99% of its steady value at 94–104% of the inner-wall τ^*_{99} (Table 2). Radial conduction across the wall is therefore completed early and does not limit the response. At steady state, 77% ($d^* = 0.2$) to 96% ($d^* = 1.0$) of the heat stored in the tube resides in the wall: a thick wall delays the interface response through its heat capacity rather than insulating it through its resistance. This capacitive character, rather than a large outer-to-inner temperature difference, is what an external sensor must contend with (Sections 3.1.3 and 3.3).

Table 2. Thermal response times of the heated-section-averaged inner-wall temperature vs. d^* ($Pe = 5, Br = 0, \phi = 0.02$).

d^*	τ^*_{50}	τ^*_{90}	τ^*_{95}	τ^*_{99}
0.2	29.0	77.7	95.6	134.6
0.4	65.0	192.4	244.9	366.2
0.8	188.1	661.9	878.3	1398.2
1.0	284.5	1070.3	1437.7	2324.3

Values are for the production time-step growth $g = 1.01$; their temporal uncertainty is 1.3–1.7% for τ^*_{99} and 0.2% for τ^*_{50}, and their spatial uncertainty below 0.3% (Section 2.6.3).

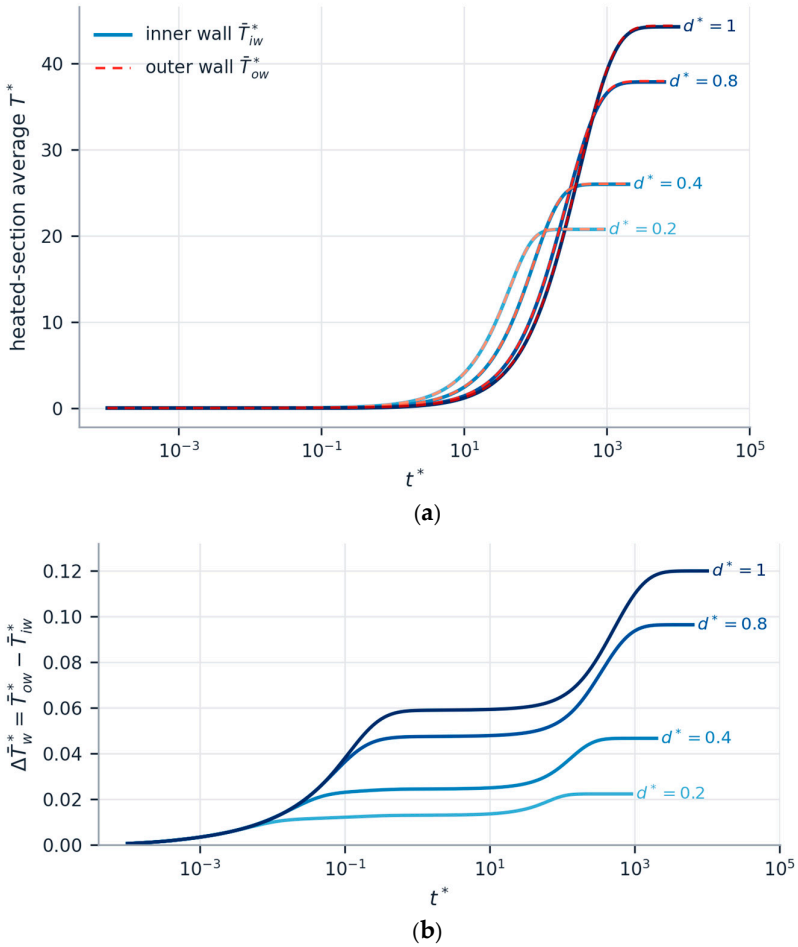


Figure 3. (**a**). Transient development of the heated-section-averaged inner-wall (solid, blue) and outer-wall (dashed, red) temperatures for $d^* = 0.2$–1.0 ($Pe = 5$, $Br = 0$, $\phi = 0.02$). The inner- and outer-wall curves are indistinguishable at this scale; their difference is resolved on its own scale in (**b**). (**b**). Difference between the two curves of (**a**): the radial temperature drop across the wall, $\Delta\bar{T}^*_w = \bar{T}^*_{ow} - \bar{T}^*_{iw}$, on its own scale (time axis identical to (**a**)). $\Delta\bar{T}^*_w$ increases monotonically for every thickness and never exceeds 0.12. The development is two-staged: a plateau at 49–58% of the steady value between $t^* \approx 0.1$–0.35 and $t^* \approx 11$–56 (radial conduction balance of the wall), followed by a second rise with the slow heating of the assembly, in which $\Delta\bar{T}^*_w$ reaches 99% of its steady value at 94–104% of the inner wall τ^*_{99} (Table 2).

3.1.2. Axial Conduction and Upstream Preheating

Axial conduction in the solid carries heat upstream of the heated zone ($x^* < 0$), warming the entering fluid before $x^* = 0$. Thicker walls provide a larger axial cross-section, so the preheating is stronger and extends further upstream, and the interface flux over the heated section becomes non-uniform, peaking near its upstream end; in this behaviour, the wall acts as a thermal buffer. This effect is quantified in Section 3.1.4.

3.1.3. Thermal Response Time and Transient Lag

The transient lag is quantified with a solver-independent metric: τ^*_p is the first time the heated-section-averaged inner-wall temperature reaches p% of its steady value, located by linear interpolation in time to remove the influence of the adaptive time-step growth. Table 2 lists the 50/90/95/99% levels, and Figure 4a shows the resulting scaling.

- Increasing d^* from 0.2 to 1.0 raises τ_{99}^* from 134.6 to 2324.3, a 17.3-fold increase (τ_{50}^*: 9.8-fold).
- Within the investigated range ($0.2 \le d^* \le 1.0$) the response time follows the empirical power law $\tau_{99}^* = 2135\,(d^*)^{1.77}$ (least-squares fit in log–log coordinates, $R^2 = 0.993$): a five-fold increase in thickness lengthens τ_{99}^* 17.3-fold, between the linear (5-fold) and quadratic (25-fold) scalings and closer to the latter. The near-quadratic growth is not a sign of radial diffusion across the wall, which is completed at $t^* \lesssim 1$ (Section 3.1.1); it is a property of the capacitive, axially conducting assembly, and Section 3.5 shows that its strength depends strongly on the wall material.
- The inner- and outer-wall response times coincide to within 0.02% at the 99% level, and under step heating the trans-wall lag (τ_{50}^* difference between the surfaces) stays below 0.41 even at $d^* = 1.0$: both surfaces follow the same slow heating of the assembly, so under a step input the trans-wall lag is too small to be distinguished from it. This motivates the frequency-domain characterisation of Section 3.3.

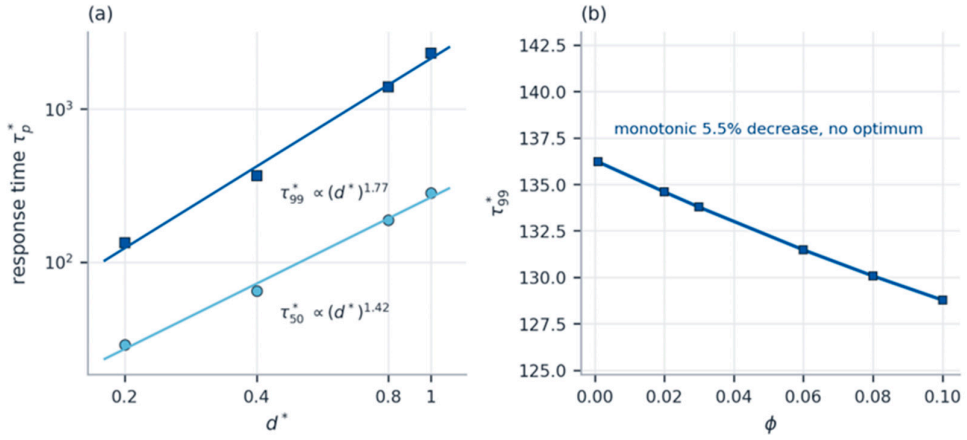


Figure 4. (**a**) Response times τ_{50}^* and τ_{99}^* vs. wall thickness ratio with power-law fits (log–log). (**b**) τ_{99}^* vs. nanoparticle volume fraction at $d^* = 0.2$ and fixed Pe: a monotonic 5.5% decrease with no interior optimum (Section 3.2.2, which also gives $d^* = 1.0$).

3.1.4. Interface Heat Flux and Nusselt Number

The interface heat flux $Q_{iw}^* = q_{iw}/q_{ow}$ (positive *into* the fluid) and Nusselt number $Nu_{iw} = 2Q_{iw}^*/(T_{iw}^* - T_b^*)$ describe how the wall redistributes the applied heating before it reaches the fluid; both are evaluated with the solid-side flux operator (Section 2.6.3). Leakage fractions below are axial integrals of Q_{iw}^* over the indicated ranges, normalised by the total interfacial heat input. T_b^* is the mixing-cup bulk temperature, velocity-weighted with the slip profile of Section 2.2.1. Table 3 summarises the steady results; Figure 5 shows the steady axial flux distributions and Figure 6 the transient Nusselt development.

Table 3. Fully developed Nusselt number, axial heat-leakage fractions and energy-closure error vs. d^* ($Pe = 5, Br = 0, \phi = 0.02$; production grid, solid-side flux operator). The analytic fully developed value is $Nu_{iw,fd} = 4.4565$ for every d^* (Section 2.6.3).

d^*	$Nu_{iw,fd}$	Upstream Leak ($x^* < 0$)	Downstream Leak ($x^* > L^*$)	Energy Closure
0.2	4.446	4.1%	0.21%	−0.04%
0.4	4.446	9.1%	0.18%	−0.04%
0.8	4.447	21.2%	0.14%	−0.04%
1.0	4.448	27.7%	0.12%	−0.05%

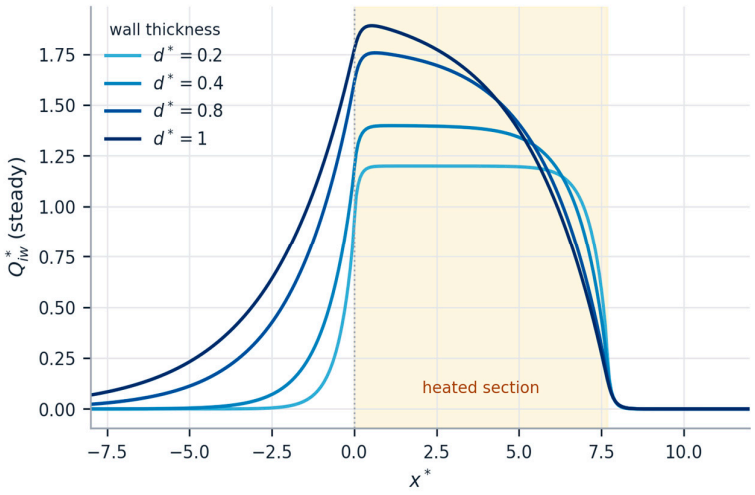


Figure 5. Steady interface heat-flux distributions $Q^*_{iw}(x^*)$ for the d^* sweep ($Pe = 5$, $Br = 0$, $\phi = 0.02$; production grid, solid-side flux operator). Upstream preheating regions ($x^* < 0$) grow with wall thickness; the shaded band marks the nominal heated section, over which the flux of the thinnest wall equals the fully developed value $1 + d^*$.

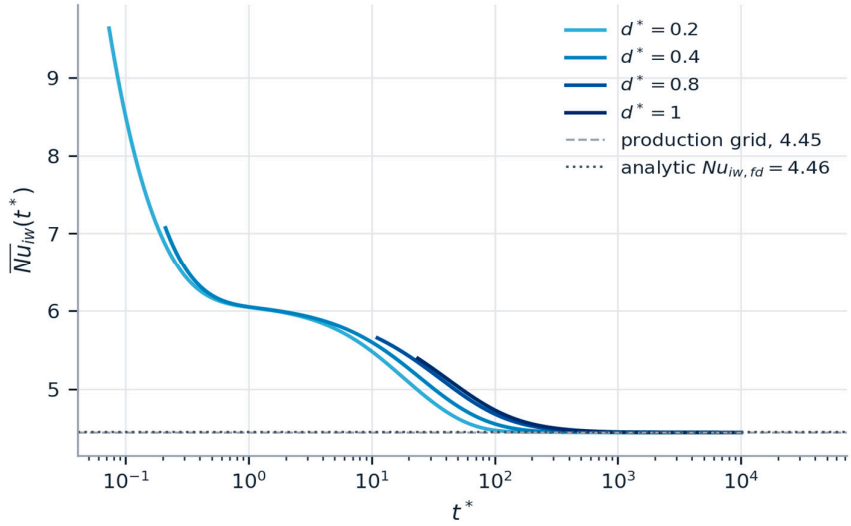


Figure 6. Mixed-mean transient Nusselt number $\overline{Nu}_{iw}(t^*)$ for the d^* sweep (production grid, solid-side flux operator; shown once the wall-to-bulk temperature difference exceeds 5% of its steady value). All thicknesses approach the steady value from above (Section 3.1.4). The dashed line marks the production-grid value 4.45, the dotted line the analytic value 4.46.

- **The fully developed Nusselt number does not depend on wall thickness.** At $Br = 0$, the analytic fully developed value depends only on the velocity profile (4.4565 for $\lambda = 0.01$); the computed values (4.446–4.448, evaluated over $3 \le x^* \le 5$) lie 0.2% below it, which is the production-grid error of Section 2.6.3. The conjugate wall changes where and when heat enters the fluid, not the developed convective coefficient. Reported microchannel Nusselt numbers have departed from conventional theory in both directions, with explanations ranging from viscous dissipation, property variation and surface roughness to experimental uncertainty [18], and axial wall conduction can bias their reduction from measurements [25,28]; in the present model,

where these effects are either absent or resolved, the fully developed value follows conventional theory for the implemented velocity profile.

- **Axial wall conduction redistributes a large fraction of the heat input.** The heat entering the fluid upstream of the heated section grows from 4.1% at $d^* = 0.2$ to 27.7% at $d^* = 1.0$, while the downstream share stays below 0.25%; at $d^* = 1.0$ more than a quarter of the heat applied over the heated section therefore enters the fluid before it. This fraction is a direct measure of the thermal-buffer role of the thick wall. The upstream preheating regions decay within the computational domain (Section 2.6.1), so the fractions are not truncated by the inlet.
- **The energy balance closes.** The deviation of $\int Q_{iw}^{*}\,\mathrm{d}x^{*}$ from the applied input $(1 + d^{*})L^{*}$ is below 0.05% for every thickness.
- **The transient Nusselt number approaches its steady value from above for every thickness** (Figure 6). Early in the transient, the thermal boundary layer is thin and $\overline{Nu}_{iw}$ is high (9.6 at the earliest evaluated time for $d^* = 0.2$); it decays to the fully developed value as the boundary layer grows, and thicker walls reach that value later, in step with their longer response times.

3.2. Effect of Nanoparticle Volume Fraction (ϕ)

The ϕ sweep (0.001–0.10, at $Pe = 5$, $Br = 0$, $d^* = 0.2$ and 1.0) isolates the effect of concentration at fixed dimensionless groups; the physically coupled behaviour at a constant flow rate is treated in Section 3.4. At fixed Pe and with the concentration-independent slip coefficient, ϕ enters the problem only through the wall-to-nanofluid ratios k_{wnf} and α_{wnf}. Between $\phi = 0.001$ and 0.10 they fall by 24% and 26% as k_{nf} rises, while the wall-to-fluid heat-capacity ratio k_{wnf}/α_{wnf} rises by 3%.

3.2.1. Interface Temperature and Heat Transfer Coefficient

Increasing ϕ from 0.001 to 0.10 lowers the steady inner-wall temperature in the nanofluid scale by 1.7% at $d^* = 0.2$ and by 4.7% at $d^* = 1.0$. The convective structure is unchanged: with a concentration-independent slip coefficient, the fully developed Nusselt number does not depend on ϕ (4.446 on the production grid). The dimensional heat transfer coefficient $h = Nu_{iw}\,k_{nf}/D_i$ therefore rises in proportion to the conductivity, by a factor of 1.32 at $\phi = 0.10$; the gain comes entirely from the conductivity, not from any change in the flow structure.

3.2.2. Effect on the Transient Response Time

Table 4 lists the response times over the ϕ sweep for a thin and a thick wall; Figure 4b shows the thin-wall trend.

Table 4. Thermal response times of the heated-section-averaged inner-wall temperature vs. ϕ ($Pe = 5, Br = 0$) for $d^* = 0.2$ and 1.0.

ϕ	τ_{50}^{*} (0.2)	τ_{90}^{*} (0.2)	τ_{95}^{*} (0.2)	τ_{99}^{*} (0.2)	τ_{50}^{*} (1.0)	τ_{99}^{*} (1.0)
0.001	29.1	78.2	96.4	136.2	290.4	2410.0
0.02	29.0	77.7	95.6	134.6	284.5	2324.3
0.03	29.0	77.4	95.2	133.8	281.5	2280.1
0.06	29.0	76.7	94.0	131.5	272.8	2152.6
0.08	28.9	76.3	93.4	130.1	267.5	2072.3
0.10	28.9	76.0	92.8	128.8	262.4	1996.1

- **At fixed Pe, loading accelerates the response monotonically: weakly for the thin wall and markedly for the thick wall.** Between $\phi = 0.001$ and 0.10, τ_{99}^{*} falls by 5.5% at $d^* = 0.2$ and by 17.2% at $d^* = 1.0$ (τ_{50}^{*}: 0.6% and 9.6%); there is no

interior extremum in either case. The thick wall responds more strongly because its transient is dominated by the wall (Section 3.1.1), whose coupling to the fluid changes with ϕ through k_{wnf} and α_{wnf}. These values are insensitive to the slip model (Section 2.2.1).

- **The fixed-Pe sweep isolates the mathematical effect of concentration.** Because $t^* = \alpha_{nf}\, t/R_i^2$ contains the nanofluid diffusivity, which rises by 36% at $\phi = 0.10$, the dimensional response at a fixed flow rate must be read from the coupled simulations of Section 3.4 rather than from Table 4.

3.3. System-Level Thermal Filtering: Frequency Response

Section 3.1.3 showed that under a *step* change, the inner- and outer-wall response times are nearly identical, so a step input cannot separate the filtering across the wall from that of the assembly as a whole. To separate them, the outer-wall heat flux is modulated sinusoidally about the steady state, $q^*(t^*) = 1 + \varepsilon\sin(\omega t^*)$, and the amplitude and phase of the resulting inner- and outer-wall temperature oscillations are determined. Two transfer characteristics are distinguished: the *system* response, from the outer heat-flux input to the inner-wall temperature, and the *trans-wall* response, from the outer-wall to the inner-wall temperature.

Because the properties are temperature-independent, the discrete energy equations are linear. Writing the semi-discrete system as $\boldsymbol{M}\,\mathrm{d}\boldsymbol{T}/\mathrm{d}t^* + \boldsymbol{K}\boldsymbol{T} = \boldsymbol{f} + \varepsilon\sin(\omega t^*)\,\boldsymbol{f}_q$, with $\boldsymbol{f}_q$ the heating part of the source, the periodic response is $\boldsymbol{T}(t^*) = \boldsymbol{T}_{ss} + \mathrm{Im}[\hat{\boldsymbol{T}}\, e^{i\omega t^*}]$ with

$$(i\omega\,\boldsymbol{M} + \boldsymbol{K})\,\hat{\boldsymbol{T}} = \varepsilon\,\boldsymbol{f}_q. \tag{17}$$

This complex linear system is solved directly (Section 2.6.1) at any ω. The time-domain alternative consists of integrating over several forcing cycles and demodulating the final ones; compared with it, the present route removes three error sources: the inner-iteration lag of Section 2.6.2, the temporal discretisation error (backward Euler with 40 steps per period replaces $i\omega$ by $(1 - e^{-i\omega\Delta t^*})/\Delta t^*$, which under-predicts the amplitude by up to 4.4% and the phase lag by up to 4.8° over the present range), and the start-up cycles. The frequency-domain solution was verified against direct time integration at $d^* = 0.4$, $\omega = 0.02$ (eight cycles, $\varepsilon = 0.1$, lock-in demodulation of the final four; domain of the tolerance study of Section 2.6.2): with the same time step, the GPU solver at $\delta_{\mathrm{it}} = 10^{-8}$ gives an amplitude ratio of 0.4758 and a phase of −62.41°, against 0.4760 and −62.38° from the frequency-domain solution with the backward-Euler symbol; the two agree to within 0.05% and 0.03°. Linearity also makes the result independent of ε.

The system response is normalised by the quasi-static response of the heating-driven part of the field, $|H_{\mathrm{sys}}| = A_{T_{iw}}/(\varepsilon\,\bar{T}_q)$, where $\bar{T}_q$ is the heated-section-averaged inner-wall temperature produced by the heating alone ($\boldsymbol{K}\boldsymbol{T}_q = \boldsymbol{f}_q$), so that $|H_{\mathrm{sys}}| \to 1$ as $\omega \to 0$; at $Br = 0$, $\bar{T}_q$ is the full steady temperature. The *wall* transfer function $|H_w| = A_{T_{iw}}/A_{T_{ow}}$ isolates the filtering by the solid between its two surfaces.

Table 5 lists the system amplitude ratio and phase at five frequencies for four wall thicknesses; Table 6 gives the cut-off frequencies ($|H_{\mathrm{sys}}| = 1/\sqrt{2}$), and Figure 7 shows the continuous Bode diagrams over $10^{-4} \le \omega \le 3$.

Table 5. System frequency response at the inner wall (frequency-domain solution; $Pe = 5$, $Br = 0$, $\phi = 0.02$).

d^*	Quantity	$\omega = 0.005$	0.01	0.02	0.05	0.1
0.2	$\lvert H_{\mathrm{sys}}\rvert$	0.989	0.957	0.845	0.460	0.208
0.2	phase (°)	−10.3	−20.4	−38.9	−73.7	−84.1
0.4	$\lvert H_{\mathrm{sys}}\rvert$	0.929	0.774	0.495	0.194	0.096
0.4	phase (°)	−23.9	−43.1	−66.3	−83.1	−85.8

0.8	$\lvert H_{\mathrm{sys}}\rvert$	0.584	0.349	0.184	0.075	0.038
0.8	phase (°)	−52.4	−68.4	−78.9	−84.9	−87.0
1.0	$\lvert H_{\mathrm{sys}}\rvert$	0.431	0.247	0.130	0.053	0.027
1.0	phase (°)	−60.0	−72.2	−80.2	−85.3	−87.5

Table 6. Cut-off frequency ($\lvert H_{\mathrm{sys}}\rvert = 1/\sqrt{2}$), frequency of $-45°$ phase, product with the step response time (τ^*_{99} extrapolated to $g \to 1$), and wall transfer function at $\omega = 1$.

d^*	ω_c	$\omega_{-45°}$	$\omega_c\tau^*_{99}$	$\lvert H_w\rvert(\omega = 1)$
0.2	0.0299	0.0237	3.96	0.998
0.4	0.0121	0.0106	4.36	0.993
0.8	0.00353	0.00377	4.88	0.962
1.0	0.00218	0.00256	5.03	0.928

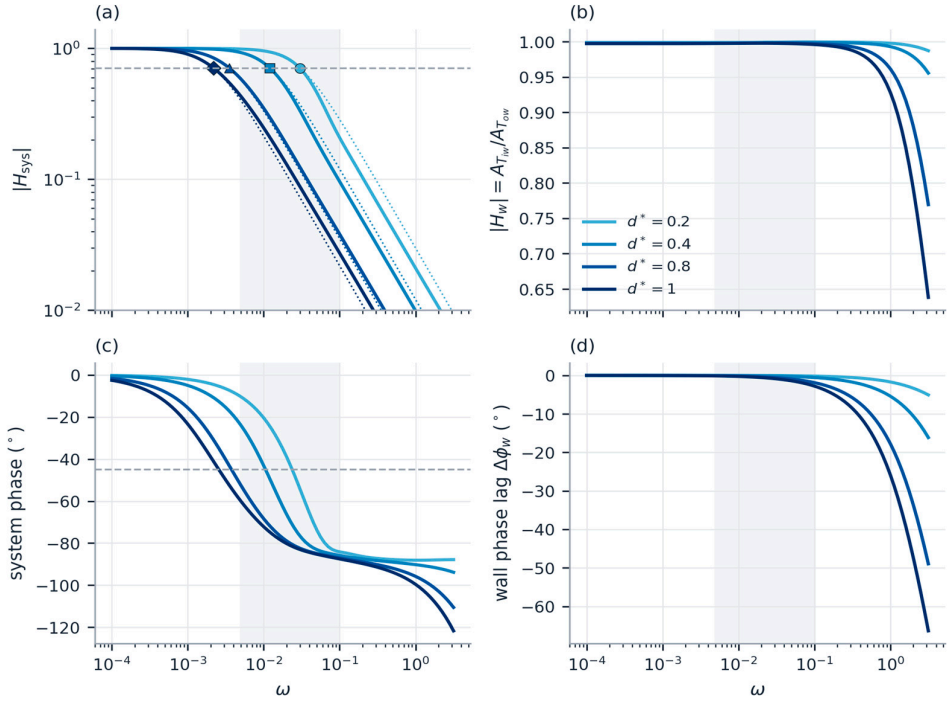


Figure 7. Frequency response computed in the frequency domain (continuous curves, $10^{-4} \le \omega \le 3$; $Pe = 5$, $Br = 0$, $\phi = 0.02$): (**a**) system amplitude ratio $\lvert H_{\mathrm{sys}}\rvert$ with the $1/\sqrt{2}$ cut-off level (dashed line), whose intersections with the curves (markers) give the cut-off frequencies ω_c of Table 6, and single-pole reference curves (dotted); (**b**) wall transfer function $\lvert H_w\rvert$; (**c**) system phase with the −45° level (dashed line), whose intersections give $\omega_{-45°}$ of Table 6; (**d**) wall phase lag $\Delta\phi_w$. The shaded band marks the frequency range of Table 5 ($0.005 \le \omega \le 0.1$). Below $\omega \approx 0.1$ the wall is radially quasi-static ($\lvert H_w\rvert \ge 0.996$): the attenuation in (**a**) is capacitive.

Four findings emerge:

- **The assembly is a strong low-pass filter whose bandwidth is set by the wall thickness.** $\lvert H_{\mathrm{sys}}\rvert$ falls monotonically with both ω and d^*; at $d^* = 1.0$, $\omega = 0.1$ only 2.7% of the quasi-static amplitude survives. The cut-off follows $\omega_c \approx 0.00238\,(d^*)^{-1.62}$ ($R^2 = 0.99$) over the studied range: doubling the wall thickness reduces the usable bandwidth about threefold. Near the cut-off, the response is close to single-pole (dotted curves in Figure 7a; the $-45°$ frequency lies between $0.79\,\omega_c$ and $1.17\,\omega_c$), and above it the amplitude rolls off at about -20 dB per decade. The phase, however, does not saturate at $-90°$: at $\omega = 1$ it reaches $-88°$ ($d^* = 0.2$) to

$-100°$ ($d^* = 1.0$), the additional lag coming from conduction across the wall, which becomes visible in $|H_w|$ at the same frequencies.

- **The harmonic and step characterisations are consistently linked.** The product $\omega_c \tau_{99}^*$ is 3.96, 4.36, 4.88 and 5.03 for $d^* = 0.2,0.4,0.8,1.0$. It stays within 14% of $\ln(100) \approx 4.6$, the value of an ideal single-pole system, so the cut-off and the response time probe the same dominant thermal time scale by independent routes. Its systematic increase with d^*, from 14% below to 9% above $\ln(100)$, shows that the response is not strictly single-pole; the product is therefore reported as an empirical link, not an identity.
- **In this frequency range the wall is radially quasi-static, not a trans-wall filter.** For $\omega \leq 0.1$, $|H_w| \geq 0.996$ and $|\Delta\phi_w| \leq 2.8°$ (both extremes at $d^* = 1.0$, $\omega = 0.1$): the two wall faces oscillate essentially together. The attenuation above is therefore not a diffusive amplitude loss between the outer and inner surfaces but a capacitive, system-level effect: the wall loads the system as a thermal mass. This is consistent with the small steady radial drop and the early radial balance of the wall (Section 3.1.1, Figure 3b). Genuine trans-wall filtering sets in only at $\omega \sim 1$, some 30–460 times ω_c, where $|H_w|$ falls to 0.998, 0.993, 0.962 and 0.928 for $d^* = 0.2,0.4,0.8,1.0$ (Table 6).
- **Implication for outer-wall sensing.** An outer-surface measurement is amplitude-faithful to the interface at these frequencies ($|H_w| \approx 1$), but the system suppresses all spectral content above ω_c, and ω_c shrinks rapidly with wall thickness. Fast interior events thus leave an attenuated, phase-lagged, near-threshold signature on any external sensor, which is the physical basis for model-based (or learning-based) reconstruction of the inner-wall state from outer-wall histories, the subject of a companion study (cf. the hybrid numerical–machine-learning framework of [43]).

3.4. Coupled Operating Points at Constant Flow Rate

The sweeps of Sections 3.1 and 3.2 treat Pe, Br, ϕ and d^* as independent to isolate their effects. In a loop operated at a constant flow rate (constant mean velocity u_m) and heater flux, however, the nanofluid properties shift the active groups (Section 2.5); Table 7 gives this shift under the Maiga correlations. Increasing ϕ from 0.001 to 0.10 reduces Pe by 26%, because the conductivity gain outweighs the slight heat-capacity drop, and raises Br, which is purely viscous, 2.96-fold; the latter matters only in the high-dissipation limit of Section 3.6.

Table 7. Property scaling and active dimensionless-parameter shift vs. ϕ (constant velocity u_m and flux q''; Pe_0 and Br_0 refer to the pure base fluid).

ϕ	k_{nf}/k_{bf}	μ_{nf}/μ_{bf}	$(\rho C_p)_{nf}/(\rho C_p)_{bf}$	Pe/Pe_0	Br/Br_0
0.001	1.003	1.007	1.000	0.997	1.007
0.03	1.086	1.330	0.992	0.913	1.330
0.06	1.181	1.881	0.984	0.833	1.881
0.08	1.249	2.371	0.978	0.783	2.371
0.10	1.322	2.960	0.973	0.736	2.960

Simulations were performed at six concentrations along this constant-flow-rate trajectory ($Pe = 4.99 \rightarrow 3.68$, $Br = 0$, $d^* = 0.2$ and 1.0). The heated length was kept at $L^* = 7.68$ as in the rest of the study, so the dimensional heater length, $R_i\, Pe\, L^*$, scales with Pe. Because t^* and T^* are scaled with nanofluid properties, the results are converted to base-fluid scales ($T^*\, k_{bf}/k_{nf}$, $t^*\, \alpha_{bf}/\alpha_{nf}$) so that different concentrations are compared at the same physical time and temperature (Table 8).

Table 8. Coupled operating points at constant flow rate and heater flux, relative to $\phi = 0.001$ ($Br = 0$; base-fluid scales; values in parentheses are d^*). h, W and PEC are given for $d^* = 0.2$; at $d^* = 1.0$ they differ by at most 0.004. The τ_{99} and T_{iw} ratios refer to the fixed dimensionless heater length $L^* = 7.68$, i.e., to a dimensional heater length proportional to Pe (Section 3.4).

ϕ	Pe	τ_{99} (0.2)	τ_{99} (1.0)	T_{iw} (0.2)	T_{iw} (1.0)	h/h_0	W/W_0	PEC
0.02	4.71	0.976	1.001	0.955	0.960	1.054	1.186	0.995
0.03	4.57	0.964	1.002	0.932	0.940	1.083	1.320	0.987
0.06	4.16	0.931	1.005	0.867	0.880	1.178	1.867	0.957
0.08	3.92	0.913	1.007	0.827	0.842	1.246	2.354	0.937
0.10	3.68	0.896	1.009	0.789	0.806	1.318	2.938	0.921

- **Response time.** In base-fluid time, the thin-wall response is about 10% faster at $\phi = 0.10$, whereas the thick-wall response is unchanged (+0.9%). The base-fluid-scale inner-wall temperature falls to 0.79 ($d^* = 0.2$) and 0.81 ($d^* = 1.0$) of its $\phi = 0.001$ value. Both ratios refer to the fixed dimensionless heater length $L^* = 7.68$.
- **Heat transfer coefficient.** Because $Nu_{iw,fd}$ does not change with ϕ, h rises in proportion to k_{nf}, by a factor of 1.32 at $\phi = 0.10$; this ratio does not depend on the heater length.
- **Pumping-power penalty.** For the fully developed slip flow, the pressure gradient at a constant flow rate is proportional to $\mu_{nf}/(1 + 4\lambda)$ (Section 2.2.1), so with the concentration-independent slip coefficient the pumping power W rises with the viscosity ratio, 2.94-fold at $\phi = 0.10$. A Webb-type performance evaluation criterion [69], here in the form $\mathrm{PEC} = (h/h_0)/(W/W_0)^{1/3}$, decreases monotonically with loading, from 0.995 at $\phi = 0.02$ to 0.92 at $\phi = 0.10$: at a constant flow rate and under the Maiga correlations, the conductivity gain does not compensate for the viscosity increase by this criterion. The verdict depends on the criterion: with the friction-factor ratio in place of W/W_0 the same ratio stays between 1.00 and 1.02, because the denser nanofluid has a lower friction factor at the same velocity. The pumping-power form is used here because, at a fixed flow rate, W is the power that the pump must actually supply.
- **Comparison at equal physical devices.** Because L^* is fixed, Table 8 does not compare physically identical devices: at $\phi = 0.10$ the heater is 26% shorter ($Pe = 3.68$ instead of 4.99) and, at the same flux q'', receives 26% less heat than at $\phi = 0.001$. The heat transfer coefficient, the pumping power and the PEC do not depend on the heater length, so their ratios also hold for identical devices. The temperature and response-time ratios do depend on it. By the energy balance, at the same q'' and u_m the bulk temperature rise over the heater is proportional to $L/(\rho C_p)_{nf}$. At fixed L^* ($L \propto Pe \propto (\rho C_p)_{nf}/k_{nf}$) it therefore scales as k_{bf}/k_{nf} (0.76 at $\phi = 0.10$), which explains the fall of T_{iw} to 0.79–0.81, whereas for an equal physical heater it scales as $(\rho C_p)_{bf}/(\rho C_p)_{nf}$ (1.03), and the conductivity gain then reduces only the wall-to-bulk temperature difference. The lower wall temperature in Table 8 therefore reflects mainly the smaller heat input of the shorter heater rather than better cooling of an equal device. The shorter heater also shortens the transit time over the heated section, so part of the faster thin-wall response may likewise stem from it. The τ_{99} and T_{iw} ratios of Table 8, and the τ_{99} ratios of Section 3.6, thus describe the fixed-L^* comparison and should not be read as the gain of an equal physical device.

3.5. Sensitivity to Wall Material and Peclet Number

The results of Sections 3.1–3.4 are for the generic wall of the reference study [36], whose volumetric heat capacity is ten times that of water; that of common wall materials is 0.3–0.9 times that of water. The step and frequency analyses were therefore repeated

for three wall materials used in microfluidic devices: borosilicate glass, stainless steel (AISI 304) and PDMS, the standard material of soft-lithography devices [70]. Glass and steel take their properties at 300 K from [44]; for PDMS (Sylgard 184), $k_s = 0.2$ W/(m K) and $\rho_s = 1030$ kg/m³ are taken from the manufacturer's data sheet [71] and $(C_p)_s = 1460$ J/(kg K) from the Polymer Data Handbook [72]. In addition, the generic wall was run at $Pe = 2.5$ and 10. All cases use $Br = 0$ and $\phi = 0.02$; for each, the inlet section was extended until the results were independent of it (Section 2.6.1). Table 9 and Figure 8 summarise the results.

Table 9. Sensitivity of the thickness effect to the wall material and the Peclet number ($Br = 0$, $\phi = 0.02$; $Pe = 5$ unless stated). $(\rho C_p)_s/(\rho C_p)_{bf} = k_{sf}/\alpha_{sf}$; values in parentheses are d^*; ratios are between $d^* = 1.0$ and $d^* = 0.2$; the leakage is the upstream share of the interfacial heat input at $d^* = 1.0$.

Wall	k_{sf}	α_{sf}	$(\rho C_p)_s/(\rho C_p)_{bf}$	τ^*_{99} (0.2)	τ^*_{99} (1.0)	τ^*_{99} Ratio	ω_c Ratio	Leakage
generic	10	1	10	134.6	2324.3	17.3	13.7	27.7%
steel	25.0	27.8	0.90	50.1	578.9	11.6	9.9	53.4%
glass	2.35	5.29	0.44	21.6	68.8	3.2	2.7	6.8%
PDMS	0.336	0.934	0.36	19.3	41.8	2.2	2.0	1.5%
generic, $Pe = 2.5$	10	1	10	301.5	7226.9	24.0	22.1	65.1%
generic, $Pe = 10$	10	1	10	98.1	915.7	9.3	7.9	7.5%

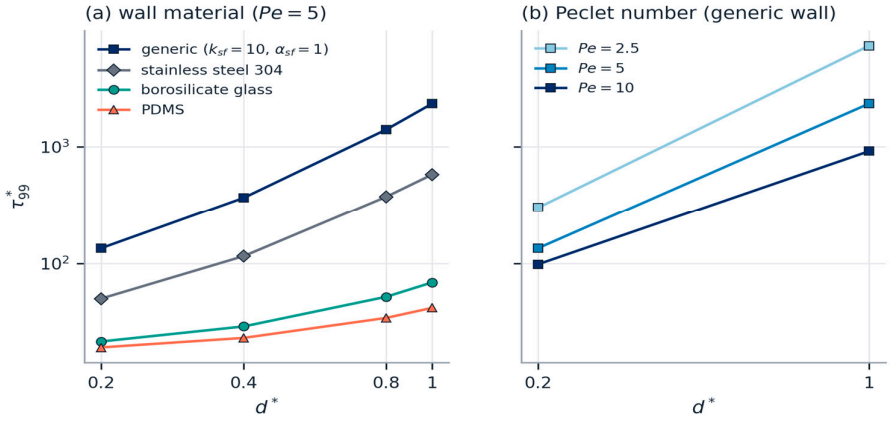


Figure 8. Sensitivity of the step response time τ^*_{99} to the wall thickness for (**a**) different wall materials at $Pe = 5$ and (**b**) different Peclet numbers for the generic wall ($Br = 0$, $\phi = 0.02$).

- **The strength of the thickness effect depends strongly on the wall material.** A five-fold increase in thickness lengthens τ^*_{99} 17-fold for the generic wall, 12-fold for stainless steel, 3-fold for glass and 2-fold for PDMS, and lowers ω_c correspondingly. Walls of low heat capacity and low conductivity, such as glass and PDMS, respond within $t^* \approx 20$–70 at every thickness, and the dominance of wall thickness found for the generic wall is obtained here only for walls whose heat capacity or conductivity is high relative to the fluid. Stainless steel, whose heat capacity is close to that of water but whose conductivity is 25 times higher, conducts more than half of the heat upstream of the heater at $d^* = 1.0$, and its response is correspondingly slower than that of glass.
- **The thickness effect weakens with increasing Pe.** The τ^*_{99} ratio is 24, 17 and 9 for $Pe = 2.5$, 5 and 10, and the upstream leakage at $d^* = 1.0$ falls from 65% to 7.5%, consistent with the reduced role of axial wall conduction at higher Pe [25].

- The conclusions on the role of the wall are therefore restricted to the simulated range of wall materials and Pe.

3.6. High-Dissipation Limit ($Br = 0.01$)

To expose the effect of viscous dissipation, which becomes significant in high-shear micro-geometries [20], the step analysis is repeated with $Br = 0.01$. This value lies far outside the microfluidic window of Section 2.4: at $Pe = 5$ it corresponds to $D_i \approx 1$ µm and $q'' \approx 14$ W/cm² (Table A4), where $\Delta T_{iw} \approx 2.3$ K and $Ri_D \sim 10^{-10}$, so the constant-property and forced-convection assumptions still hold, but the particle-to-channel size ratio (tens of nanometres to 1 µm) strains the homogeneous single-phase description. The case is therefore presented as a hypothetical upper bound of dissipation. Because the problem is linear, results for any intermediate Br follow from $T^* = T_q^* + Br\,T_d^*$, where T_d^* is the field produced by unit Br. Viscous heating also occurs upstream of the heater and is carried into it, so the results depend on where the inlet temperature is prescribed; they are reported for the inlet position of the original formulation, $x_{in}^* = -11.52$ (doubling the upstream length lengthens τ_{99}^* at $d^* = 0.2$ from 179 to 309).

At $Br = 0.01$ the dissipation contributes 10% ($d^* = 0.2$) to 5% ($d^* = 1.0$) of the steady heated-section inner-wall temperature ($H_0 = \bar{T}_q/\bar{T} = 0.902,\ 0.920,\ 0.944,\ 0.951$ for $d^* = 0.2$,0.4,0.8,1.0). On the same domain it lengthens τ_{99}^* from 134.6, 366.4, 1385.5 and 2252.5 ($Br = 0$) to 179.4, 414.4, 1415.1 and 2274.1, that is, by 33%, 13%, 2.1% and 1.0%: the effect is largest for the thin wall, where the dissipation share is largest. Along the constant-flow-rate trajectory of Section 3.4, Br rises with the viscosity from 0.0101 to 0.0296 ($Br_0 = 0.01$, same inlet position). At $\phi = 0.10$ the base-fluid-scale τ_{99} is then 0.942 ($d^* = 0.2$) and 0.949 ($d^* = 1.0$) times its $\phi = 0.001$ value, against 0.896 and 1.009 at $Br_0 = 0$ (Table 8), and the PEC falls to 0.89–0.90 instead of 0.92. The frequency response referred to the heating-driven part $\bar{T}_q$ (Section 3.3) does not depend on Br, because the dissipation source is not modulated; referred to the total mean temperature, it would tend to $H_0 < 1$ at low frequency. By linearity, at the Brinkman numbers of the microfluidic window (10^{-8}–10^{-6}, Section 2.4) the dissipation contributes about 10^{-5} or less of the wall temperature, which justifies $Br = 0$ for the main results.

4. Conclusions

Transient conjugate heat transfer of an Al_2O_3-water nanofluid in a thick-walled microtube heated over a finite length was investigated with a vertex-centred finite-volume model, solved by a sparse direct method in the time and frequency domains. The grid and time-step uncertainties of the quantities reported in Section 3 were quantified (below 0.3% and 1.3–1.7%, respectively), the iterative error was removed, and the conjugate core was validated against a reference solution. Within the simulated range ($Pe = 2.5$–10, $d^* = 0.2$–1.0, $\phi \le 0.10$, $Br = 0$ with a high-dissipation limit at $Br = 0.01$; the generic wall $k_{sf} = 10$, $\alpha_{sf} = 1$ and three real wall materials), the main conclusions are:

1. **Wall thickness acts on the transient through the heat capacity of the wall, not its resistance.** For the generic wall, raising d^* from 0.2 to 1.0 lengthens the 99% response time 17.3-fold, empirically as $(d^*)^{1.77}$, i.e., close to quadratic growth. The radial temperature drop across the wall stays below 0.3% of the wall temperature, radial conduction is completed at $t^* \lesssim 1$, and 77–96% of the stored heat resides in the wall.
2. **The strength of the thickness effect depends on the wall material and on Pe.** The ratio of τ_{99}^* between $d^* = 1.0$ and 0.2 is 17 for the generic wall, 12 for stainless steel, 3 for borosilicate glass and 2 for PDMS, and it falls from 24 to 9 as Pe rises

from 2.5 to 10. The dominance of wall thickness is therefore found only for walls whose heat capacity or conductivity is high relative to the fluid.

3. **Axial wall conduction redistributes the heat input without changing the developed Nusselt number.** The fully developed Nusselt number (4.45, within 0.2% of the analytic value) is independent of d^* and ϕ, whereas the share of the heat entering the fluid upstream of the heater grows from 4% at $d^* = 0.2$ to 28% at $d^* = 1.0$ for the generic wall (53% for stainless steel; 65% at $Pe = 2.5$).
4. **The thick-walled assembly is a capacitive, system-level low-pass filter.** The cut-off frequency falls from 0.0299 ($d^* = 0.2$) to 0.00218 ($d^* = 1.0$), approximately as $(d^*)^{-1.62}$, and $\omega_c \tau_{99}^* = 3.96$–$5.03$ lies within 14% of the single-pole value ln(100), linking the harmonic and step characterisations. Up to $\omega = 0.1$ the two wall faces oscillate together ($|H_w| \geq 0.996$, $|\Delta\phi_w| \leq 2.8°$); trans-wall filtering appears only at frequencies 30–460 times ω_c. An outer-surface sensor is therefore amplitude-faithful to the interface but cannot resolve inner-wall events faster than ω_c.
5. **Nanoparticle loading acts mainly through the conductivity.** At fixed Pe, loading up to $\phi = 0.10$ shortens τ_{99}^* by 5.5% for the thin wall and by 17% for the thick wall, with no optimum concentration. At a constant flow rate, it raises the heat transfer coefficient 1.32-fold while the pumping power rises 2.94-fold, so the pumping-power-based performance evaluation criterion falls monotonically to 0.92: under the Maiga correlations and by this criterion, the conductivity gain does not compensate for the viscosity increase (the friction-factor form stays near 1).
6. **Viscous dissipation is negligible at microfluidic scales.** In the microfluidic window ($Br = 10^{-8}$–10^{-6}) it contributes about 10^{-5} or less of the wall temperature. In the hypothetical high-dissipation limit $Br = 0.01$ it contributes 5–10% of the wall temperature and lengthens τ_{99}^* by up to 33% (thin wall); these results depend on where the inlet temperature is prescribed.

Overall, for walls of high heat capacity or conductivity, wall thickness rather than nanoparticle loading controls the transient response, and the outer wall, while a convenient sensing surface, filters and lags the inner state in a frequency-dependent way that must be accounted for in transient control. Natural extensions are property models that resolve particle size, shape and temperature; other oxide nanoparticles whose crystalline phase changes the particle properties (for example, anatase and rutile TiO_2); experiments on real wall materials; and data-driven reconstruction of the inner-wall state from outer-wall measurements.

Funding: This research received no external funding.

Data Availability Statement: The solver, the verification and analysis scripts, and the data underlying the figures and tables are openly available on Zenodo at https://doi.org/10.5281/zenodo.23598589.

Acknowledgments: During the preparation of this study, the author used Claude Code (Anthropic, version 2.1.207) and Google Antigravity IDE (Google, version 2.5.5) for the purposes of developing the analysis, verification and visualisation scripts and assisting with the writing and language editing of the manuscript. The author has reviewed and edited the output and takes full responsibility for the content of this publication.

Conflicts of Interest: The author declares no conflicts of interest.

Abbreviations

The following abbreviations are used in this manuscript:

AISI American Iron and Steel Institute

CUDA	Compute Unified Device Architecture
GCI	Grid Convergence Index
GPU	Graphics Processing Unit
LU	Lower–Upper (triangular factorisation)
PDMS	Polydimethylsiloxane
PEC	Performance Evaluation Criterion

Appendix A

The symbols used in this paper are listed in Tables A1–A3; a superscript asterisk (*) denotes a dimensionless quantity.

Table A1. Roman symbols.

Symbol	Description	Unit
$A_{T_{iw}},\ A_{T_{ow}}$	Oscillation amplitudes of the inner- and outer-wall temperature	[−]
b	Navier slip length, $b = \lambda R_i$	[m]
Br	Brinkman number, $\mu_{nf} u_m^2/(q'' R_i)$	[−]
C	Energy-consistency ratio, $(\mathrm{d}T_b^*/\mathrm{d}x^*)/Q_{iw}^*$	[−]
C_p	Specific heat capacity at constant pressure	[J/(kg · K)]
d^*	Dimensionless wall thickness ratio, d_w/R_i	[−]
d_w	Physical wall thickness	[m]
D_i	Inner diameter of the microtube, $2R_i$	[m]
$\boldsymbol{D}$	Rate-of-strain tensor, $1/2\,(\nabla \boldsymbol{u} + \nabla \boldsymbol{u}^{\mathrm{T}})$	[s^{-1}]
$\boldsymbol{e}_x$	Axial unit vector	[−]
$\boldsymbol{f},\ \boldsymbol{f}_q$	Semi-discrete source vector and its heating part (Section 3.3)	[−]
$\boldsymbol{f}_b$	Body force per unit volume	[$\mathrm{N/m^3}$]
F_s	Grid-convergence-index safety factor	[−]
g	Adaptive time-step growth factor ($\Delta t^* \leftarrow g\,\Delta t^*;\ g = 1.01$)	[−]
$\boldsymbol{g}$	Gravitational acceleration vector ($\lvert\boldsymbol{g}\rvert = 9.81\ \mathrm{m/s^2}$)	[$\mathrm{m/s^2}$]
Gr_D	Grashof number, $\lvert\boldsymbol{g}\rvert\,\beta\,(T_{iw} - T_b)\,D_i^3/\nu_{nf}^2$	[−]
h	Heat transfer coefficient, $h = Nu_{iw}\,k_{nf}/D_i$	[$\mathrm{W/(m^2 \cdot K)}$]
H_0	Dissipation-free fraction of the mean inner-wall temperature, $\bar{T}_q/\bar{T}$	[−]
H_{sys}	System transfer function, $A_{T_{iw}}/(\varepsilon\,\bar{T}_q)$ (inner-wall amplitude relative to the quasi-static response of the heating-driven field)	[−]
H_w	Wall thermal transfer function (inner/outer amplitude ratio, $\lvert H_w\rvert = A_{T_{iw}}/A_{T_{ow}}$)	[−]
k	Thermal conductivity	[W/(m · K)]
$k_{bf},\ k_{nf},\ k_p,\ k_s$	Thermal conductivity of the base fluid, nanofluid, nanoparticles and solid wall (k_{nf}/k_{bf}: Section 2.4)	[W/(m · K)]
k_{sf}	Solid-wall-to-base-fluid conductivity ratio, k_s/k_{bf}	[−]
k_{wnf}	Solid-wall-to-nanofluid conductivity ratio, k_s/k_{nf}	[−]
$\boldsymbol{K}$	Semi-discrete conduction matrix (Section 3.3)	[−]
L^*	Dimensionless heated section length ($L^* = 7.68$)	[−]
$\boldsymbol{M}$	Semi-discrete capacity matrix (Section 3.3)	[−]
$N_{r,f},\ N_{r,s}$	Radial control-volume counts in the fluid and solid regions	[−]
N_x	Total number of axial nodes (770)	[−]
$N_{x,in},\ N_{x,h},\ N_{x,out}$	Axial control-volume counts in the inlet, heated and outlet sections	[−]
Nu_{iw}	Interface (inner-wall) Nusselt number, $2\,Q_{iw}^*/(T_{iw}^* - T_b^*)$	[−]

p	Observed order of convergence of a refinement study; also the percentage level of τ_p^*	[−]
P	Pressure	[Pa]
Pe	Peclet number (diameter-based), $2\,u_m R_i/\alpha_{nf}$	[−]
Pr_{nf}	Prandtl number of the nanofluid, ν_{nf}/α_{nf}	[−]
q''	Constant outer wall heat flux	[W/m^2]
$q_{iw},\ q_{ow}$	Local heat flux at the fluid–solid interface and at the outer wall	[W/m^2]
$q^*(t^*)$	Dimensionless outer-flux modulation, $1+\varepsilon\sin(\omega t^*)$	[−]
Q_{iw}^*	Dimensionless interface heat flux, q_{iw}/q_{ow}	[−]
r	Radial coordinate	[m]
r^*	Dimensionless radial coordinate, r/R_i	[−]
R^2	Coefficient of determination of a curve fit	[−]
R_i	Inner radius of the microtube	[m]
Re_D	Reynolds number, $u_m D_i/\nu_{nf}$	[−]
Ri_D	Richardson number, Gr_D/Re_D^2	[−]
t	Time	[s]
t^*	Dimensionless time, $\alpha_{nf}\,t/R_i^2$	[−]
T	Temperature	[K]
T_{in}	Inlet temperature	[K]
T^*	Dimensionless temperature, $(T-T_{in})\,k_{nf}/(q''R_i)$	[−]
$T_{iw}^*, T_{ow}^*, T_b^*$	Inner-wall, outer-wall, and bulk dimensionless temperature	[−]
$\bar{T},\ \bar{T}_q$	Heated-section-averaged steady inner-wall temperature: total and heating-driven part	[−]
u	Axial velocity	[m/s]
$\boldsymbol{u}$	Velocity vector	[m/s]
u_m	Mean flow velocity	[m/s]
u_{slip}	Wall slip velocity, $u_{slip}=-b\,(\partial u/\partial r)_{wall}$	[m/s]
u^*	Dimensionless velocity profile, u/u_m	[−]
U_{prod}	Numerical uncertainty of the production level (Table 1)	[−]
W	Pumping power at constant flow rate, $\propto \mu_{nf}/(1+4\lambda)$ (Section 3.4)	[W]
x	Axial coordinate	[m]
x^*	Dimensionless axial coordinate (Graetz-scaled), $x/(R_i\,Pe)$	[−]
x_{in}^*, x_{out}^*	Numerical inlet/outlet coordinates (baseline $-23.04,\ 23.10$; extended inlets: Section 2.6.1)	[−]

Table A2. Greek symbols.

Symbol	Description	Unit
α	Thermal diffusivity, $k/(\rho C_p)$	[m^2/s]
$\alpha_{bf},\ \alpha_{nf},\ \alpha_s$	Thermal diffusivity of the base fluid, nanofluid and solid wall	[m^2/s]
α_{sf}	Solid-wall-to-base-fluid diffusivity ratio, α_s/α_{bf}	[−]
α_{wnf}	Solid-wall-to-nanofluid diffusivity ratio, α_s/α_{nf} (Section 2.2.2)	[−]
β	Volumetric thermal expansion coefficient of water	[K^{-1}]
δ_{it}	Absolute inner-iteration tolerance of the Jacobi solver	[−]
ΔT_{ref}	Reference temperature scale, $q''R_i/k_{nf}$	[K]
ΔT_{iw}	Steady mean inner-wall temperature rise over the heated section, $\bar{T}_q\,\Delta T_{ref}$ (Appendix B)	[K]
$\Delta\bar{T}_w^*$	Heated-section-averaged radial temperature drop across the wall, $\bar{T}_{ow}^*-\bar{T}_{iw}^*$	[−]
$\Delta\phi_w$	Phase lag of the inner-wall oscillation relative to the outer wall	[°]
ε	Modulation amplitude of the outer heat flux, $q^*(t^*)=1+\varepsilon\sin(\omega t^*)$	[−]

κ	Interfacial friction coefficient of the Navier slip condition, $b = \mu/\kappa$	[Pa · s/m]
λ	Dimensionless slip coefficient, b/R_i (held at λ_0 for all ϕ; Section 2.2.1)	[−]
λ_0	Base-fluid slip coefficient ($\lambda_0 = 0.01$)	[−]
μ	Dynamic viscosity	[Pa · s]
μ_{bf}, μ_{nf}	Dynamic viscosity of the base fluid and nanofluid (μ_{nf}/μ_{bf}: Section 2.4)	[Pa · s]
ν	Kinematic viscosity, μ/ρ	[m^2/s]
ρ	Density	[kg/m^3]
ρ_{bf}, ρ_{nf}, ρ_p	Density of the base fluid, nanofluid and nanoparticles (ρ_{nf}: Section 2.4)	[kg/m^3]
$(\rho C_p)_{bf}$, $(\rho C_p)_{nf}$, $(\rho C_p)_p$	Volumetric heat capacity of the base fluid, nanofluid and nanoparticles ($(\rho C_p)_{nf}$: Section 2.4)	[J/(m^3 · K)]
ρ_J	Spectral radius of the Jacobi iteration matrix	[−]
τ_p^*	Thermal response time: first time the heated-section-averaged inner-wall temperature reaches p% of its steady value ($p = 50,90,95,99$)	[−]
ϕ	Nanoparticle volume fraction	[−]
Φ^*	Dimensionless viscous dissipation function, $(du^*/dr^*)^2$	[−]
Φ_v	Viscous dissipation function, $2\,\boldsymbol{D}:\boldsymbol{D}$	[s^{-2}]
ω	Dimensionless angular forcing frequency (with respect to t^*)	[−]
ω_c	Cut-off frequency, $\lvert H_{\mathrm{sys}}(\omega_c)\rvert = 1/\sqrt{2}$	[−]
$\omega_{-45°}$	Frequency at which the system phase is $-45°$	[−]

Table A3. Subscripts.

Subscript	Description
bf	Base fluid (pure water)
c	Cut-off value
f	Fluid phase
fd	Fully developed value
h	Heated section
$in,\ out$	Inlet and outlet
it	Inner iteration
$iw,\ ow$	Inner (interface) and outer wall
nf	Nanofluid mixture
p	Nanoparticle phase (Al_2O_3)
q	Heating-driven part of the field (dissipation excluded)
ref	Reference scale
s	Solid wall material
$slip$	Wall slip
ss	Steady state
sys	System: outer heat flux to inner-wall temperature
w	Solid wall
0	Reference value: pure base fluid for Pe_0, Br_0 and λ_0; $\phi = 0.001$ for h_0 and W_0 (Table 8); initial value for Δt_0^*

Appendix B

Table A4. Representative dimensional scales of the baseline ($Pe = 5$, $d^* = 0.2$, $\phi = 0.02$; water properties at 20 °C; $k_{nf} = 0.629$ W/(m K), $\mu_{nf} = 1.20 \times 10^{-3}$ Pa s, $\alpha_{nf} = 1.51 \times 10^{-7}$ m^2/s, $\beta = 2.07 \times 10^{-4}$ K^{-1} [47]). $\Delta T_{iw} = \bar{T}_q^* \Delta T_{ref}$ with $\bar{T}_q^* = 20.8$; Ri_D is based on the fully developed wall-to-bulk temperature difference. The last row corresponds to the high-dissipation limit $Br = 0.01$.

D_i (μm)	u_m (mm/s)	Flow Rate (μL/min)	q'' (W/cm^2)	ΔT_{ref} (K)	ΔT_{iw} (K)	Br	Ri_D
50	15.1	1.78	1	0.40	8.3	1.1×10^{-6}	9.5×10^{-5}

100	7.56	3.56	1	0.80	16.5	1.4×10^{-7}	1.5×10^{-3}
100	7.56	3.56	0.3	0.24	5.0	4.6×10^{-7}	4.6×10^{-4}
200	3.78	7.13	1	1.59	33.1	1.7×10^{-8}	2.4×10^{-2}
1	756	0.036	13.7	0.11	2.3	1.0×10^{-2}	2×10^{-10}

Appendix C

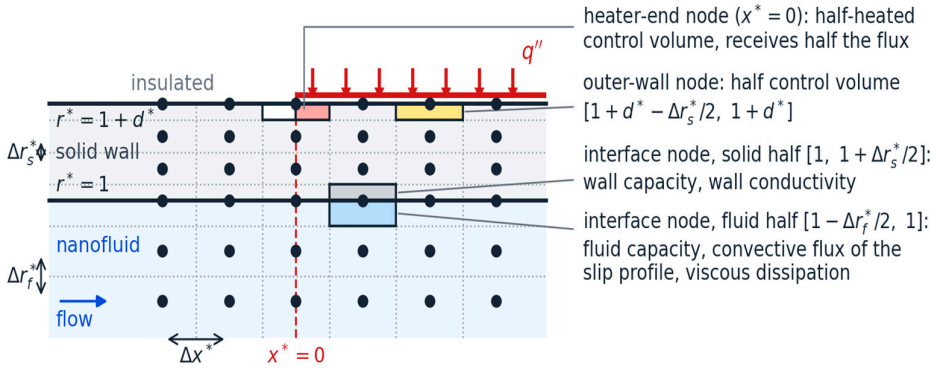


Figure A1. Vertex-centred control volumes of the discretisation of Section 2.6.1 near the start of the heated section (schematic, not to scale). Nodes lie on the grid-line intersections; each control volume is bounded by the mid-planes to its neighbours. An interface node on $r^* = 1$ carries a fluid half, $[1 - \Delta r_f^*/2,\ 1]$, with the fluid capacity, the convective flux of the slip profile and the viscous dissipation, and a solid half, $[1,\ 1 + \Delta r_s^*/2]$, with the wall capacity; the radial fluxes on either side use the conductivity of their own material. A node on the outer wall carries a half control volume, $[1 + d^* - \Delta r_s^*/2,\ 1 + d^*]$, over which its capacity, the conduction through its inner face and the applied flux are balanced. The node at the heater end $x^* = 0$ (and likewise at $x^* = L^*$) has a control volume that is only half heated and receives half the flux.

References

1. Liu, M.; Sun, J.; Sun, Z.; Xiao, Y.; Chen, Y.; Li, J.; Yu, X. A review of microfluidic technologies for thermal management in flexible electronics. *Lab Chip* **2026**, *26*, 1417–1443. https://doi.org/10.1039/D5LC00906E.
2. Tovar, S.; Hernández, C.A.; Osma, J.F. Design, Simulation, and Fabrication of a Copper–Chrome-Based Glass Heater Integrated into a PMMA Microfluidic System. *Micromachines* **2021**, *12*, 1067. https://doi.org/10.3390/mi12091067.
3. Tuckerman, D.B.; Pease, R.F.W. High-performance heat sinking for VLSI. *IEEE Electron Device Lett.* **1981**, *2*, 126–129. https://doi.org/10.1109/EDL.1981.25367.
4. Choi, S.U.S.; Eastman, J.A. Enhancing Thermal Conductivity of Fluids with Nanoparticles. In Proceedings of the ASME International Mechanical Engineering Congress and Exposition, San Francisco, CA, USA, 12–17 November 1995; pp. 99–105. https://doi.org/10.1115/IMECE1995-0926.
5. Buongiorno, J. Convective Transport in Nanofluids. *J. Heat Transf.* **2006**, *128*, 240–250. https://doi.org/10.1115/1.2150834.
6. Pak, B.C.; Cho, Y.I. Hydrodynamic and heat transfer study of dispersed fluids with submicron metallic oxide particles. *Exp. Heat Transf.* **1998**, *11*, 151–170. https://doi.org/10.1080/08916159808946559.
7. Das, S.K.; Putra, N.; Thiesen, P.; Roetzel, W. Temperature Dependence of Thermal Conductivity Enhancement for Nanofluids. *J. Heat Transf.* **2003**, *125*, 567–574. https://doi.org/10.1115/1.1571080.
8. Xuan, Y.; Li, Q. Investigation on Convective Heat Transfer and Flow Features of Nanofluids. *J. Heat Transf.* **2003**, *125*, 151–155. https://doi.org/10.1115/1.1532008.
9. Wen, D.; Ding, Y. Experimental investigation into convective heat transfer of nanofluids at the entrance region under laminar flow conditions. *Int. J. Heat Mass Transf.* **2004**, *47*, 5181–5188. https://doi.org/10.1016/j.ijheatmasstransfer.2004.07.012.
10. Beck, M.P.; Yuan, Y.; Warrier, P.; Teja, A.S. The effect of particle size on the thermal conductivity of alumina nanofluids. *J. Nanopart. Res.* **2009**, *11*, 1129–1136. https://doi.org/10.1007/s11051-008-9500-2.
11. Kilic, I.; Güneş, A.; Barut, C.; Erdoğan, B.; Yaman, O.; Topuz, A. Nanoparticle Size Effects on Thermal Conductivity of Hybrid Nanofluids: Experiments and Neural Network Modeling. *Crystals* **2026**, *16*, 651. https://doi.org/10.3390/cryst16100651.

12. Timofeeva, E.V.; Routbort, J.L.; Singh, D. Particle shape effects on thermophysical properties of alumina nanofluids. *J. Appl. Phys.* **2009**, *106*, 014304. https://doi.org/10.1063/1.3155999.
13. Maïga, S.E.B.; Palm, S.J.; Nguyen, C.T.; Roy, G.; Galanis, N. Heat transfer enhancement by using nanofluids in forced convection flows. *Int. J. Heat Fluid Flow* **2005**, *26*, 530–546. https://doi.org/10.1016/j.ijheatfluidflow.2005.02.004.
14. Ruvo, T.H.; Shuvo, M.S.; Saha, S. Revisiting thermo-physical property models of Al_2O_3-water nanofluid for natural convective flow. *Heliyon* **2024**, *10*, e26964. https://doi.org/10.1016/j.heliyon.2024.e26964.
15. Maïga, S.E.B.; Nguyen, C.T.; Galanis, N.; Roy, G. Heat transfer behaviours of nanofluids in a uniformly heated tube. *Superlattices Microstruct.* **2004**, *35*, 543–557. https://doi.org/10.1016/j.spmi.2003.09.012.
16. Baig, M.F.; Chen, G.M.; Tso, C.P. The Thermal Performance Analysis of an Al_2O_3-Water Nanofluid Flow in a Composite Micro-channel. *Nanomaterials* **2022**, *12*, 3821. https://doi.org/10.3390/nano12213821.
17. Aydın, O.; Avcı, M. Viscous-dissipation effects on the heat transfer in a Poiseuille flow. *Appl. Energy* **2006**, *83*, 495–512. https://doi.org/10.1016/j.apenergy.2005.03.003.
18. Morini, G.L. Single-phase convective heat transfer in microchannels: A review of experimental results. *Int. J. Therm. Sci.* **2004**, *43*, 631–651. https://doi.org/10.1016/j.ijthermalsci.2004.01.003.
19. Tunc, G.; Bayazitoglu, Y. Heat transfer in microtubes with viscous dissipation. *Int. J. Heat Mass Transf.* **2001**, *44*, 2395–2403. https://doi.org/10.1016/S0017-9310(00)00298-2.
20. Koo, J.; Kleinstreuer, C. Viscous dissipation effects in microtubes and microchannels. *Int. J. Heat Mass Transf.* **2004**, *47*, 3159–3169. https://doi.org/10.1016/j.ijheatmasstransfer.2004.02.017.
21. Barletta, A.; Celli, M.; Brandão, P. Wall roughness and viscous dissipation effects in microchannel heat sinks with semicircular cross-section. *Int. J. Heat Mass Transf.* **2026**, *254*, 127623. https://doi.org/10.1016/j.ijheatmasstransfer.2025.127623.
22. Neto, C.; Evans, D.R.; Bonaccurso, E.; Butt, H.-J.; Craig, V.S.J. Boundary slip in Newtonian liquids: A review of experimental studies. *Rep. Prog. Phys.* **2005**, *68*, 2859–2897. https://doi.org/10.1088/0034-4885/68/12/R05.
23. Lauga, E.; Brenner, M.; Stone, H. Microfluidics: The No-Slip Boundary Condition. In *Springer Handbook of Experimental Fluid Mechanics*; Springer: Berlin/Heidelberg, Germany, 2007; pp. 1219–1240. https://doi.org/10.1007/978-3-540-30299-5_19.
24. Avcı, M.; Aydın, O.; Arıcı, M.E. Conjugate heat transfer with viscous dissipation in a microtube. *Int. J. Heat Mass Transf.* **2012**, *55*, 5302–5308. https://doi.org/10.1016/j.ijheatmasstransfer.2012.05.038.
25. Maranzana, G.; Perry, I.; Maillet, D. Mini- and micro-channels: Influence of axial conduction in the walls. *Int. J. Heat Mass Transf.* **2004**, *47*, 3993–4004. https://doi.org/10.1016/j.ijheatmasstransfer.2004.04.016.
26. Bilir, Ş. Laminar flow heat transfer in pipes including two-dimensional wall and fluid axial conduction. *Int. J. Heat Mass Transf.* **1995**, *38*, 1619–1625. https://doi.org/10.1016/0017-9310(94)00269-2.
27. Weigand, B.; Gassner, G. The effect of wall conduction for the extended Graetz problem for laminar and turbulent channel flows. *Int. J. Heat Mass Transf.* **2007**, *50*, 1097–1105. https://doi.org/10.1016/j.ijheatmasstransfer.2006.06.047.
28. Mitra, I.; Ghosh, I. Analytical Study on Intricacies of Axial Conduction in Microchannel Heat Sinks. *J. Heat Transf.* **2022**, *144*, 094502. https://doi.org/10.1115/1.4054772.
29. Gupta, S.; Subbarao, P.M.V. Experimental investigation of conjugate heat transfer in nanofluid-cooled microchannel heat sink to mitigate back axial conduction at low Reynolds numbers. *J. Therm. Anal. Calorim.* **2025**, *150*, 5751–5774. https://doi.org/10.1007/s10973-025-14136-5.
30. Jamali, J.A. Conjugate heat transfer analysis of single-bubble growth in microchannel flow boiling with varying wall thicknesses and materials. *Heat Mass Transf.* **2026**, *62*, 148. https://doi.org/10.1007/s00231-026-03784-4.
31. Lin, T.F.; Kuo, J.C. Transient conjugated heat transfer in fully developed laminar pipe flows. *Int. J. Heat Mass Transf.* **1988**, *31*, 1093–1102. https://doi.org/10.1016/0017-9310(88)90097-X.
32. Yan, W.M.; Tsay, Y.L.; Lin, T.F. Transient conjugated heat transfer in laminar pipe flows. *Int. J. Heat Mass Transf.* **1989**, *32*, 775–777. https://doi.org/10.1016/0017-9310(89)90225-1.
33. Olek, S.; Elias, E.; Wacholder, E.; Kaizerman, S. Unsteady conjugated heat transfer in laminar pipe flow. *Int. J. Heat Mass Transf.* **1991**, *34*, 1443–1450. https://doi.org/10.1016/0017-9310(91)90287-O.
34. Schutte, D.J.; Rahman, M.M.; Faghri, A. Transient conjugate heat transfer in a thick-walled pipe with developing laminar flow. *Numer. Heat Transf. Part A* **1992**, *21*, 163–186. https://doi.org/10.1080/10407789108944871.
35. Bilir, Ş. Transient conjugated heat transfer in pipes involving two-dimensional wall and axial fluid conduction. *Int. J. Heat Mass Transf.* **2002**, *45*, 1781–1788. https://doi.org/10.1016/S0017-9310(01)00270-8.

36. Ateş, A.; Darıcı, S.; Bilir, Ş. Unsteady conjugated heat transfer in thick walled pipes involving two-dimensional wall and axial fluid conduction with uniform heat flux boundary condition. *Int. J. Heat Mass Transf.* **2010**, *53*, 5058–5064. https://doi.org/10.1016/j.ijheatmasstransfer.2010.07.059.
37. Darıcı, S.; Bilir, Ş.; Ateş, A. Transient conjugated heat transfer for simultaneously developing laminar flow in thick walled pipes and minipipes. *Int. J. Heat Mass Transf.* **2015**, *84*, 1040–1048. https://doi.org/10.1016/j.ijheatmasstransfer.2014.12.049.
38. Conti, A.; Lorenzini, G.; Jaluria, Y. Transient conjugate heat transfer in straight microchannels. *Int. J. Heat Mass Transf.* **2012**, *55*, 7532–7543. https://doi.org/10.1016/j.ijheatmasstransfer.2012.07.046.
39. Rahman, M.E.; Weibel, J.A. Influence of convective heat transfer and wall thermal capacity on dynamic interactions between wall temperature and pressure drop oscillations during microchannel flow boiling. *Int. J. Heat Mass Transf.* **2024**, *221*, 125111. https://doi.org/10.1016/j.ijheatmasstransfer.2023.125111.
40. Shah, Q.; Almakki, M.; Radwan, T.; Khider, M.E.; Shah, S.A. Impact of Oscillatory Conditions on Thermal Enhancement in Nanofluid Flow Through Porous Media. *Crystals* **2026**, *16*, 632. https://doi.org/10.3390/cryst16100632.
41. Altun, A.H.; Bilir, Ş.; Ateş, A. Transient conjugated heat transfer in thermally developing laminar flow in thick walled pipes and minipipes with time periodically varying wall temperature boundary condition. *Int. J. Heat Mass Transf.* **2016**, *92*, 643–657. https://doi.org/10.1016/j.ijheatmasstransfer.2015.09.011.
42. Beck, J.V.; Blackwell, B.; St. Clair, C.R., Jr. *Inverse Heat Conduction: Ill-Posed Problems*; Wiley-Interscience: New York, NY, USA, 1985.
43. Ates, M.S.; Akpinar, E.; Kaymak, C.; Das, M. Hybrid numerical–machine learning framework for heat transfer prediction in TiO_2 nanofluid microtubes. *J. Eng. Res.* **2026**, *14*, 659–680. https://doi.org/10.1016/j.jer.2025.12.007.
44. Bergman, T.L.; Lavine, A.S.; Incropera, F.P.; DeWitt, D.P. *Fundamentals of Heat and Mass Transfer*, 7th ed.; John Wiley & Sons: Hoboken, NJ, USA, 2011.
45. Ge, Z.; Cahill, D.G.; Braun, P.V. Thermal Conductance of Hydrophilic and Hydrophobic Interfaces. *Phys. Rev. Lett.* **2006**, *96*, 186101. https://doi.org/10.1103/PhysRevLett.96.186101.
46. Bejan, A. *Convection Heat Transfer*, 4th ed.; John Wiley & Sons: Hoboken, NJ, USA, 2013. https://doi.org/10.1002/9781118671627.
47. Wagner, W.; Pruß, A. The IAPWS Formulation 1995 for the Thermodynamic Properties of Ordinary Water Substance for General and Scientific Use. *J. Phys. Chem. Ref. Data* **2002**, *31*, 387–535. https://doi.org/10.1063/1.1461829.
48. Moshizi, S.A.; Malvandi, A.; Ganji, D.D.; Pop, I. A two-phase theoretical study of Al_2O_3–water nanofluid flow inside a concentric pipe with heat generation/absorption. *Int. J. Therm. Sci.* **2014**, *84*, 347–357. https://doi.org/10.1016/j.ijthermalsci.2014.06.012.
49. Malvandi, A.; Ganji, D.D. Mixed Convection of Alumina/Water Nanofluid in Microchannels using Modified Buongiorno's Model in Presence of Heat Source/Sink. *J. Appl. Fluid Mech.* **2016**, *9*, 2277–2289. https://doi.org/10.18869/acadpub.jafm.68.236.25641.
50. Bilir, Ş.; Ateş, A. Transient conjugated heat transfer in thick walled pipes with convective boundary conditions. *Int. J. Heat Mass Transf.* **2003**, *46*, 2701–2709. https://doi.org/10.1016/S0017-9310(03)00032-2.
51. Khanafer, K.; Vafai, K. A critical synthesis of thermophysical characteristics of nanofluids. *Int. J. Heat Mass Transf.* **2011**, *54*, 4410–4428. https://doi.org/10.1016/j.ijheatmasstransfer.2011.04.048.
52. Batchelor, G.K. The effect of Brownian motion on the bulk stress in a suspension of spherical particles. *J. Fluid Mech.* **1977**, *83*, 97–117. https://doi.org/10.1017/S0022112077001062.
53. Einstein, A. Eine neue Bestimmung der Moleküldimensionen. *Ann. Phys.* **1906**, *324*, 289–306. https://doi.org/10.1002/andp.19063240204.
54. Brinkman, H.C. The viscosity of concentrated suspensions and solutions. *J. Chem. Phys.* **1952**, *20*, 571. https://doi.org/10.1063/1.1700493.
55. Sundar, L.S.; Sharma, K.V.; Ramanathan, S. Experimental investigation of heat transfer enhancements with Al_2O_3 nanofluid and twisted tape insert in a circular tube. *Int. J. Nanotechnol. Appl.* **2007**, *1*, 21–28.
56. Maxwell, J.C. *A Treatise on Electricity and Magnetism*, 2nd ed.; Clarendon Press: Oxford, UK, 1881.
57. Hamilton, R.L.; Crosser, O.K. Thermal conductivity of heterogeneous two-component systems. *Ind. Eng. Chem. Fundam.* **1962**, *1*, 187–191. https://doi.org/10.1021/i160003a005.
58. Buongiorno, J.; Venerus, D.C.; Prabhat, N.; McKrell, T.; Townsend, J.; Christianson, R.; Tolmachev, Y.V.; Keblinski, P.; Hu, L.-W.; Alvarado, J.L.; et al. A benchmark study on the thermal conductivity of nanofluids. *J. Appl. Phys.* **2009**, *106*, 094312. https://doi.org/10.1063/1.3245330.
59. Corcione, M. Empirical correlating equations for predicting the effective thermal conductivity and dynamic viscosity of nanofluids. *Energy Convers. Manag.* **2011**, *52*, 789–793. https://doi.org/10.1016/j.enconman.2010.06.072.

60. Duan, F.; Kwek, D.; Crivoi, A. Viscosity affected by nanoparticle aggregation in Al_2O_3-water nanofluids. *Nanoscale Res. Lett.* **2011**, *6*, 248. https://doi.org/10.1186/1556-276X-6-248.
61. Wang, J.; Yang, X.; Klemeš, J.J.; Tian, K.; Ma, T.; Sunden, B. A review on nanofluid stability: Preparation and application. *Renew. Sustain. Energy Rev.* **2023**, *188*, 113854. https://doi.org/10.1016/j.rser.2023.113854.
62. Squires, T.M.; Quake, S.R. Microfluidics: Fluid physics at the nanoliter scale. *Rev. Mod. Phys.* **2005**, *77*, 977–1026. https://doi.org/10.1103/RevModPhys.77.977.
63. Huber, M.L.; Perkins, R.A.; Laesecke, A.; Friend, D.G.; Sengers, J.V.; Assael, M.J.; Metaxa, I.N.; Vogel, E.; Mareš, R.; Miyagawa, K. New International Formulation for the Viscosity of H_2O. *J. Phys. Chem. Ref. Data* **2009**, *38*, 101–125. https://doi.org/10.1063/1.3088050.
64. Roache, P.J. Perspective: A method for uniform reporting of grid refinement studies. *J. Fluids Eng.* **1994**, *116*, 405–413. https://doi.org/10.1115/1.2910291.
65. Celik, I.B.; Ghia, U.; Roache, P.J.; Freitas, C.J.; Coleman, H.; Raad, P.E. Procedure for estimation and reporting of uncertainty due to discretization in CFD applications. *J. Fluids Eng.* **2008**, *130*, 078001. https://doi.org/10.1115/1.2960953.
66. Virtanen, P.; Gommers, R.; Oliphant, T.E.; Haberland, M.; Reddy, T.; Cournapeau, D.; Burovski, E.; Peterson, P.; Weckesser, W.; Bright, J.; et al. SciPy 1.0: Fundamental algorithms for scientific computing in Python. *Nat. Methods* **2020**, *17*, 261–272. https://doi.org/10.1038/s41592-019-0686-2.
67. Li, X.S. An overview of SuperLU: Algorithms, implementation, and user interface. *ACM Trans. Math. Softw.* **2005**, *31*, 302–325. https://doi.org/10.1145/1089014.1089017.
68. Ates, M.S. *Code and Data for: Transient Thermophysical Response of Al_2O_3 Nanoparticle-Loaded Fluids in Thick-Walled Microtubes: Conjugate Heat Transfer and System-Level Thermal Filtering*; Zenodo: Meyrin, Switzerland, 2026. https://doi.org/10.5281/zenodo.23598589.
69. Webb, R.L. Performance evaluation criteria for use of enhanced heat transfer surfaces in heat exchanger design. *Int. J. Heat Mass Transf.* **1981**, *24*, 715–726. https://doi.org/10.1016/0017-9310(81)90015-6.
70. McDonald, J.C.; Whitesides, G.M. Poly(dimethylsiloxane) as a Material for Fabricating Microfluidic Devices. *Acc. Chem. Res.* **2002**, *35*, 491–499. https://doi.org/10.1021/ar010110q.
71. Dow Corning Corporation. *SYLGARD 184 Silicone Elastomer: Product Information*; Form No. 06-1009-01; Dow Corning Corporation: Midland, MI, USA.
72. Mark, J.E. (Ed.) *Polymer Data Handbook*; Oxford University Press: New York, NY, USA, 1999.

Disclaimer/Publisher's Note: The statements, opinions and data contained in all publications are solely those of the individual author(s) and contributor(s) and not of MDPI and/or the editor(s). MDPI and/or the editor(s) disclaim responsibility for any injury to people or property resulting from any ideas, methods, instructions or products referred to in the content.